Eidgenössische Technische Hochschule Zürich
Swiss Federal Institute of Technology Zurich

Advanced Power Semiconductor
Laboratory

Bachelor's Thesis

Anlaysis of simulation methods of ion implantation depth profiles in 4H-SiC

Inés Martí Hidalgo

Supervised by:
Manuel Belanche Guadas

June 6, 2022

ETH zürich

APS

Analysis of simulation methods of ion implantation depth profiles in 4H-SiC

Bachelor's Thesis (Spring 2022)

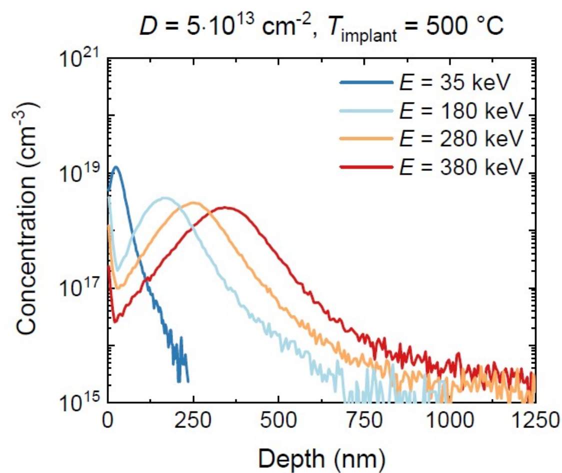

Fig. 1: Depth profiles of phosphorous ions implanted into 4H-SiC with different kinetic energies. From: J. Mueting, PhD thesis, ETH Zurich, 2019.

Introduction

In silicon carbide (SiC), doping of selected areas of the semiconductor is achieved by ion implantation. At dedicated implantation facilities, ions such as Al or P are accelerated to a well-defined kinetic energy and implanted into the semiconductor. After activation annealing, each dopant atom can provide an electron or a hole to its vicinity, hence modifying the conductivity of the semiconductor. Since the shape and the doping concentration of the implanted regions are critical for the the performance of the final SiC device, a thorough understanding of the relationship between implantation energy and depth distribution is required.

Scope of the Thesis

The aim of this project is to analyse different software and methods for the simulation of implantation processes into the SiC crystal. This is achieved by completing the following tasks:

- Getting familiarized with the existing program based on statistical methods developed at APS $(10\,\%)$.
- Implementation of an extended version of statistical methods $(30\,\%)$.
- Set-up of ion implantation simulations using Monte-Carlo-based tools $(30\,\%)$.
- Evaluation and comparison of statistical and physical methods $(30\,\%)$.

Contact For more details please contact:

Supervisors:	Manuel Belanche Guadas	belanche@aps.ee.ethz.ch	ETL F24.1
Professor:	Prof. Dr. U. Grossner	ulrike.grossner@ethz.ch	ETL F 28

Abstract

Low diffusion coefficients of silicon carbide (SiC) make of ion implantation the prevalent technique for doping of this wide bandgap semiconductor. The need for optimal processes during manufacturing of power electronic devices, stresses the need of high-accuracy simulation of ion implantation depth profiles. Furthermore, upcoming technologies like CoolMOS transistors demand of precise control over the doping process, which involves high energy ion implantation.

This thesis analyses some of the main alternatives for the prediction of implantation depth profiles. The statistical models, characterised by low computational costs and limited flexibility and precision, were defined and compared to SIMS measurements. This project also covers the evaluation of physical models, which usually provide more exact predictions at the expense of higher computational costs. The results given by different simulators will be discussed and compared to empirical data in order to find the optimal alternative for predicting high energy ion implantation depth profiles.

Eidgenössische Technische Hochschule Zürich
Swiss Federal Institute of Technology Zurich

Declaration of originality

The signed declaration of originality is a component of every semester paper, Bachelor's thesis, Master's thesis and any other degree paper undertaken during the course of studies, including the respective electronic versions.

Lecturers may also require a declaration of originality for other written papers compiled for their courses.

I hereby confirm that I am the sole author of the written work here enclosed and that I have compiled it in my own words. Parts excepted are corrections of form and content by the supervisor.

Title of work (in block letters):

Analysis of simulation methods of ion implantation depth profiles in 4H-SiC

Authored by (in block letters):

For papers written by groups the names of all authors are required.

Name(s):	First name(s):
Martí Hidalgo	Inés

With my signature I confirm that

- I have committed none of the forms of plagiarism described in the 'Citation etiquette' information sheet.
- I have documented all methods, data and processes truthfully.
- I have not manipulated any data.
- I have mentioned all persons who were significant facilitators of the work.

I am aware that the work may be screened electronically for plagiarism.

Place, date	Signature(s)
Zürich, 06.06.2022	

For papers written by groups the names of all authors are required. Their signatures collectively guarantee the entire content of the written paper.

Acknowledgement

Firstly, I would like to express my deepest gratitude to Prof. Dr. Ulrike Grossner for giving me the opportunity of doing my bachelor thesis at the Advanced Power Semiconductor Laboratory.

I am also extremely grateful for all the help and guidance that my supervisor Manuel Belanche provided throughout all the project, always available to solve the complications that arose along the way. He also gave me the chance to incorporate my ideas while proposing his own, working in a cooperative way that was truly enriching.

Many thanks to other students and workers at the APS Laboratory that have offered help in many occasions and created a welcoming and friendly atmosphere to work in.

Lastly, I would like to extend my sincere thanks to my family and friends for offering their unconditional support and encouragement to be my best self.

Contents

Project Description III

Abstract V

Declaration of Originality VII

List of Figures XIII

1 Introduction 1
1.1 Motivation . . . 1
1.2 Thesis organization . . . 4

2 Background on Ion Implantation 5
2.1 Ion stopping . . . 5
2.1.1 Historic introduction . . . 5
2.1.2 Stopping power . . . 6
2.1.3 Nuclear stopping . . . 7
2.1.4 Electronic stopping . . . 10
2.2 Ion channeling . . . 12
2.3 Implantation-induced damage . . . 15

3 Simulation of Ion Implantation 19
3.1 Statistical models . . . 19
3.1.1 Pearson IV distribution . . . 20
3.1.2 Dual Pearson distribution . . . 23
3.2 Physical models . . . 25
3.2.1 SIIMPL: Simulation of Ion Implantation . . . 26
3.2.2 SRIM: Stopping and Range of Ions in Mater . . . 30
3.2.3 TCAD: Sentaurus . . . 32

4 Discussion of Results and Comparison between Simulators 37
4.1 Performance of *Implantor.m* . . . 37
4.2 Performance of a dual Pearson based simulator . . . 41
4.3 Performance of SIIMPL . . . 47
4.4 Performance of SRIM . . . 50

4.5 Performance of TCAD: *Sentaurus Process* 53

5 Conclusion and Outlook **57**

Bibliography **59**

Appendix A **A1**
A.1 Implantor.m A1
A.2 Algorithm based on the dual Pearson A7
A.3 *Sentaurus Process* A14

List of Figures

1.1 Structure of a CoolMOS using a planar gate [4]. 2
1.2 Effect of charge imbalance in the breakdown voltage for different values of charge Q [5]. 3
1.3 On-resistance vs blocking voltage curve for superjunction and conventional devices in different materials, i.e. Si, SiC and GaN [4]. 4

2.1 Energy dependence of stopping cross-sections for ^{14}N in SiC. Nuclear cross-section, S_n, is represented by a broken line and electronic cross-section, S_e, by a solid line. The Fermi velocity v_F, and the Thomas-Fermi velocity v_{TF}, are shown as vertical solid and dotted lines, respectively [2]. 6
2.2 Geometry of a two-body collision between a moving particle M_1 and a stationary one M_2 following the principle of binary collision approximation (BCA) [13]. 8
2.3 Ratio of electronic stopping and ion velocity S_e/v as a function of Z_1 for SiC (•) and C (∘), obtained from experimental data. S_e/v predicted by Lindhard and Scharf (LS) theory is shown with a solid line in the case of SiC, and a broken line in the case of C. Also, calculations with Density Functional Theory (DTF) can be seen in the graph (×) [2]. 11
2.4 Sketch of a random ion trajectory (blue) and a channeled ion (red) in a crystalline structure. 12
2.5 Crystallographic structure for some of the preferred directions for ion channeling in 4H-SiC. Si atoms are represented in blue, while C atoms are orange [13]. 13
2.6 Dependence of ion channeling on the position of the incident ion in the plane perpendicular to the channel. Typical trajectories for ions implanted into an atom wall (1), close to it (2) and into the center of the channels (3), are depicted. 14
2.7 MC-BCA simulation of the damage cascade created by a single 100 keV Al (•) ion implanted in 4H-SiC. C and Si interstitials are represented as (•) and (•) respectively, while C and Si vacancies are shown as (•) and (•) [2]. 16

3.1 Comparison of Al depth profiles obtained from SIMS measurements (∘), their linear fit to a Pearson function (solid lines) and the profiles calculated from Eqs. 3.7 with the fitting parameters given in Table 3.1 (broken lines) [8]. 23
3.2 Comparison between BCA simulations, Pearson IV and dual Pearson fittings to depth profiles of Al implantation in 4H-SiC [29]. 25
3.3 Schematic representation of consecutive binary collisions between an ion I and target atoms A and B. 27
3.4 Representation of the effect of thermal vibrations in the lattice atoms by displacing them a)closer or b)further away from the incoming ion [2]. . . . 28
3.5 Depth profiles given by MARLOWE (broken lines) and SIIMPL (solid lines) algorithms for a 100 keV X implantation into the $< 001 >$ direction for a single cubic target. On the left the simulation was performed without including thermal vibrations. On the right, displacements of 0.01Å are added [2]. 29
3.6 Results given by a SRIM simulation of Al implantation into SiC at 380 keV. The four first distribution moments are also obtained in the simulation. 32
3.7 Comparison of the depth profiles obtained from Al implantation into 4H-SiC at 450 keV and doses of 2.5 and 25 $\times 10^{13}$ cm^{-2} [35]. 34

4.1 Comparison of SIMS measurements (solid lines) [13] against *Implantor.m* simulations (broken lines). Figure (a) depicts the effect of energy in Al implantation into 4H-SiC and a dose $D = 5e14$ cm^{-2}. Figure (b) shows the dose dependence of Al implantation into 4H-SiC at 280 keV. 38
4.2 Comparison of ion implantation depth profiles given by: *Sentaurus Process*, SRIM and *Implantor.m*. Simulation conditions were Al implantation into 4H-SiC, with energy $E = 8$ MeV and dose $D = 5e14$ cm^{-2}. 39
4.3 Comparison of the predictions given by *Sentaurus Process* and *Implantor.m* in 4H-SiC for a high temperature Al implantation. Simulations were performed for $T = 500°C$, energy $E = 8$ MeV and dose $D = 5e15$ cm^{-2}. 40
4.4 Comparison of depth profiles predicted by *Sentaurus Process*, SRIM, and *Implantor.m* for a high energy Al implantation into 4H-SiC. The simulations were performed under an energy $E = 20$ MeV and dose $D = 5e12$ cm^{-2}. 41
4.5 Profile of Al implantation into 4H-SiC, with energy $E = 300$ keV and dose $D = 5e15$ cm^{-2}, given by an algorithm based on the dual Pearson. Pearson 1 refers to the fraction of randomly moving ions and Pearson 2 refers to channeled and backscattered ions. Final profile is the sum of both distributions. 42

4.7 Comparison between depth profiles of Al implantations into 4H-SiC given by a dual Pearson based simulator (broken lines) and SIMS (solid lines) [13]. Implantation was performed for different energies (35 kev, 180 keV) and a dose $D = 5e14\ cm^{-2}$. 44
4.8 Evaluation of the dose dependence in SIMS [13] (solid lines) and dual Pearson (broken lines) depth profiles of Al implantation into 4H-SiC, at 280 keV. 44
4.9 Comparison of depth profiles resulting from Al implantation into 4H-SiC, at 110 keV and a dose $D = 7e13\ cm^{-2}$. BCA [37], Pearson IV [2] and dual Pearson simulations are represented. 45
4.10 Depth profiles resulting of Al implantation simulations into 4H-SiC, at 220 keV and a dose $D = 1e14\ cm^{-2}$. BCA [37], *Implantor.m* and dual Pearson simulations are represented. 46
4.11 Comparison of SIMS measurements [8] (solid line) and a dual Pearson based simulation (broken line) of Al implantation into 4H-SiC with energy $E = 1$ MeV and dose $D = 2.6e13\ cm^{-2}$. 47
4.12 Influence of energy in depth profiles of Al implantation into 4H-SiC with a dose $D = 5e14\ cm^{-2}$. SIIMPL simulations are represented by broken lines, while SIMS [13] measurements are represented by solid lines. . . . 48
4.13 Representation of Al implantation into 4H-SiC at 280 keV and different doses. Depth profiles were obtained by SIMS measurements [13] (solid lines) and SIIMPL simulations (broken lines). 49
4.14 Depth profiles of Al implantation into 4H-SiC given by SIMS [13] (solid lines) and TRIM simulations (broken lines). Implantation was performed at different energies and a dose $D = 5e14\ cm^{-2}$. 50
4.15 Depth profiles given by Al implantation into 4H-SiC at 280 keV and different doses measured with SIMS [13] in solid lines. Broken lines represent the simulation by TRIM of implantation in the same conditions. 51
4.16 Depth profiles of Al implantation into 4H-SiC at different energies and a dose $D = 2.6e13\ cm^{-2}$. SIMS measurements [8] are represented by solid lines and TRIM simulations by broken lines. 52
4.17 Depth profiles of Al implantation into 4H-SiC by SIMS [13], represented by solid lines, and *Sentaurus Process* in broken lines. Implantation was performed for different energies and a dose of $D = 5e14\ cm^{-2}$. 53
4.18 Comparison of results given by *Sentaurus Process* (broken lines) and SIMS measurements [13] (solid lines) for an Al implantations into 4H-SiC. The dose dependence is reflected by maintaining the energy constant at $E = 280$ keV and adjusting the implanted dose. 54

4.19 Comparison of depth profiles given by *Sentaurus Process* simulations (broken lines) and SIMS measurements [8] (solid lines) for Al implantation into 4H-SiC in the high energy range. Implantation was performed for different energies and a dose $D = 2.6e13\ cm^{-2}$. 55
4.20 Comparison of ion implantation depth profiles for an Al implantation into 4H-SiC given by TCAD (*Sentaurus Process*), SRIM and SIIMPL simulations (broken lines). SIMS measurement [13] of the corresponding implantation is also represented in the graph with a solid line. Implantation conditions were: energy $E = 380$ keV and dose $D = 5e14\ cm^{-2}$. 56

Chapter 1

Introduction

1.1 Motivation

Upcoming trends and technologies require the optimisation of current power electronics, in which semiconductors play a key role. Intensive research is being carried out in semiconductor devices towards improving efficiency by reducing dissipation losses, following Moore's miniaturization law and optimizing switching behaviour. Traditional materials like silicon have undergone a huge development over the last decades. However, as they reach maturity and face their material limitations, new options such as wide bandgap semiconductors are taking a bigger role in the industry, offering superior properties in comparison to silicon . Among them, silicon carbide and gallium nitride stand out. While both are next generation materials, they present different characteristics that make them suitable for specific applications. This thesis will be focused on the study of the former.

The larger distance between valence and conduction bands allows silicon carbide to operate at higher voltages, frequencies and temperatures. The wide bandgap together with its exceptional thermal conductivity leads to smaller dissipation losses. Therefore, silicon carbide devices are reduced in size and allow smaller and lighter cooling components [1]. Moreover, this material is especially hard and wear resistant, which makes it convenient for a wide range of applications [2].

On the other hand, silicon carbide is rarely present in nature and it needs to be synthesized. Due to the infancy of this material, processing is still complex and costly, and it currently undergoes an acute evolution. All of this together explains that this material does not match cost efficiency of traditional silicon technology. Thus, great efforts are being made in this field in order to reduce this drawback and eventually substitute silicon by silicon carbide.

One of the main challenges that arises is silicon carbide doping for the final acquisition of electronic devices. In the same way as silicon, SiC belongs to the group-IV semiconductors, which are mainly doped positively by group-III atoms and negatively by group-V atoms. Primarily, silicon carbide p-doping relies on the use of B and Al, while n-doping is usually carried out with N and P. Different techniques are available to dope SiC samples, like doping during the growth process and diffusion from the

sample surface [2]. However, the need for selective and precise doping and the low diffusion coefficient of SiC make of ion implantation the optimal doping method for this material. Nevertheless, a reasonable amount of challenges are linked to this technique and need to be tackled in order to make the most of SiC. High annealing temperatures (1500-1600ºC) are required in order to obtain a reasonable amount of activation and to restore implantation-induced damage such as point defects and dislocation loops [3], which lead to some undesirable effects, e.g. high reverse leakage current or surface roughness [1]. In these regard, high-temperature ion implantation is being explored as a way of avoiding the aforesaid lattice damage and its consequent complications.

The final goal is being able to process state-of-the-art devices that respond to current needs. Since the invention of the transistor several derivations have been developed and, among them superjunction MOSFETs stand out.

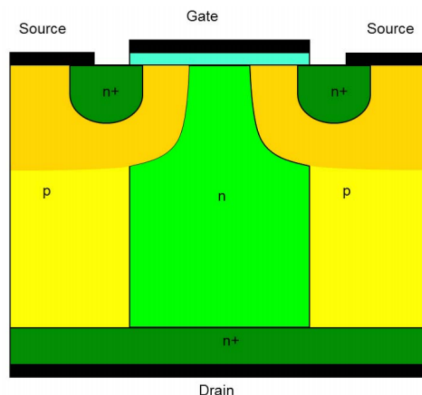

Fig. 1.1: Structure of a CoolMOS using a planar gate [4].

This innovative structure is considered one of the greatest contributions to power electronics since the development of insulated gate bipolar transistor (IGBT) [4]. Superjunction technology, which is the base for commercially relevant devices known as CoolMOS, offers much lesser on-resistance while maintaining a high breakdown voltage. In order to achieve this, the drift region is divided in highly doped alternate p/n trenches or pillars [5] as shown in Fig. 1.1. To advantage from this configuration, the charge in the p and n region should be exactly balanced, otherwise the electric field would lose its desirable uniformity and consequently, breakdown voltage would diminish [4], [6]. This effect is depicted in Fig. 1.2, where for perfectly balanced structures the breakdown voltage presents a maximum. As charge difference between the p and n regions increases, the breakdown voltage decreases. The rate at which the breakdown voltage is affected by the charge imbalance is more pronounced for higher values of charge.

Although this goal is rather unrealistic, great progress is being made in this field and better results are noticeable. This technology holds a promising future with the

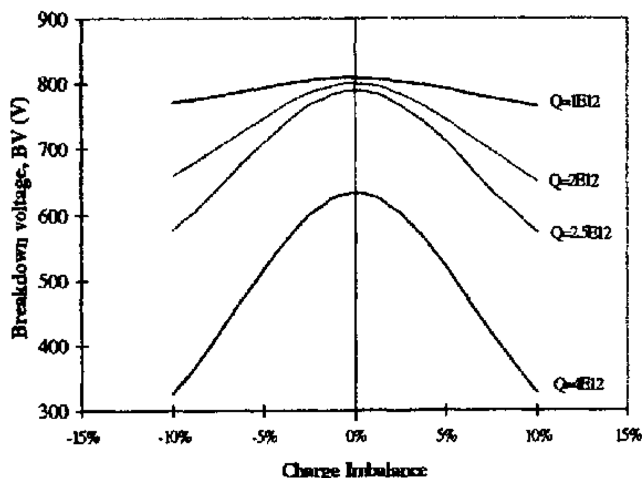

Fig. 1.2: Effect of charge imbalance in the breakdown voltage for different values of charge Q [5].

incorporation of state-of-the-art materials like SiC and GaN, which have already shown outstanding performances (see Fig.1.3).

In order to optimise so said challenges and reach SiC technology sophistication there is still a long way to go and further investigation and optimisation of fabrication processes are required. This thesis aims in that direction by analysing the characteristics of different simulation algorithms of ion implantation depth profiles. Accurate predictions by these algorithms would result in cost and time savings, which is precisely a critical point in SiC devices, since they offer great properties with the downside of being highly expensive.

Stief et al. [7] proposed a fitting of range profiles based on the Pearson VI statistical distribution for a given set of energies, which was supported later on by Janson [8]. However, this models did not represent asymmetries of the distributions. That led to thinking that the combination of two weighted Pearson functions could describe more accurately implantation profiles. Although improvements in comparison to the single Pearson approach are observed, this model is constrained by considerable limitations. Monte-Carlo based simulators rooted in physical phenomena come closer to profiles obtained from secondary ion mass spectrometry (SIMS). This thesis will evaluate the possibilities of SIIMPL (Simulation of Ion Implantation) [2], SRIM [9] and the widespread TCAD software, where a broad spectrum of implantation conditions, species and simulation options are available.

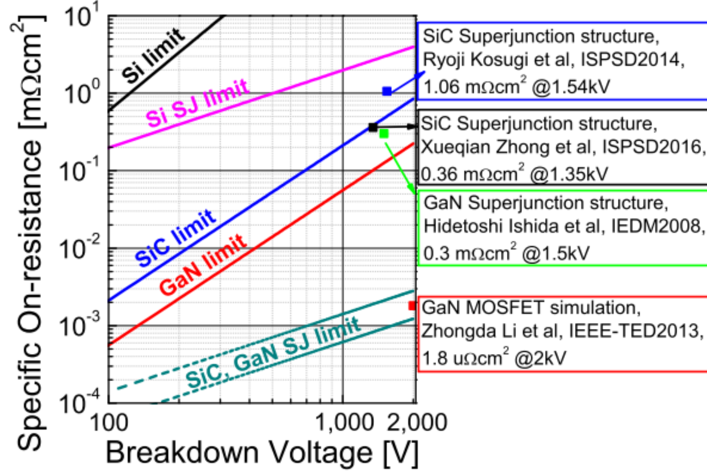

Fig. 1.3: On-resistance vs blocking voltage curve for superjunction and conventional devices in different materials, i.e. Si, SiC and GaN [4].

1.2 Thesis organization

The increased interest in wide bandgap semiconductors calls for new efficient simulation technologies that allow the optimization of the manufacturing process of power electronics devices. The analysis of current alternatives for simulating ion implantation depth profiles falls within the scope of this thesis, which will particularly evaluate their performance for SiC with a stronger emphasis on the high energy range.

In order to properly analyze the limitations and advantages of the proposed simulators, one needs to understand the physical phenomena behind ion implantation. On that note, Chapter 2 gives a theoretical background on ion stopping and some of the crucial phenomena that influence depth profiles, i.e. the channeling effect and implantation-induced damage. Chapter 3 gives an insight into the characteristics of simulators based on statistical and physical models. Within these groups, a set of programs are proposed and evaluated individually. Then, they will be compared against each other in Chapter 4, which will state their strengths and weaknesses in light of simulation results and SIMS measurements given as reference. Lastly, a brief summary of the results obtained from this thesis is given in Chapter 5, together with an outlook on the different directions for improving the simulation of ion implantation depth profiles.

Chapter 2

Background on Ion Implantation

In order to move towards silicon carbide total integration in power electronics technology, some challenges and open questions need to be solved. With ion implantation being one of the main processing steps of power electronics devices, its optimization becomes critical. In addition to implantation techniques, powerful simulation programs need to be implemented to reduce costs and time. For this purpose, complete understanding of implantation phenomena must be achieved. This is precisely the aim of this chapter, which will introduce the background theory related with this topic.

2.1 Ion stopping

2.1.1 Historic introduction

When an impinging ion penetrates a solid target it undergoes a series of interactions with the atoms and electrons present in the substrate. The ion gradually loses its energy due to these collisions until it eventually stops. The theoretical understanding of this matter dates back to J.J Thomson's study of scattering of two point charges, followed by Rutherford's theories on backscattering. Bohr's contribution was also significant. He suggested that the energy loss of ions moving through a solid was based on two mechanisms: nuclear stopping and electronic stopping. Later on, Bethe and Bloch investigated the behaviour of light and fast particles moving in the 10 MeV/amu - 2 GeV/amu velocity range [10]. On the other hand, Fermi and Teller concluded that slow energy particles stopping was proportional to the particle's speed. The estimation of a screened Coulomb potential and the corresponding screening function was deduced by Bohr and Firsov following different methods. Great contributions were made by Lindhard, Scharff and Schiott unifying a stopping and range theory (LSS-theory) that estimated stopping powers with a high degree of accuracy, specially for low energy heavy ions. With development of computers, the Hartree-Fock atom was introduced and improvements were made as a contribution of Rousseas, Chu and Powers in electronic stopping, and Wilspon, Haggmark and Biersack in nuclear stopping [10]. The calculation of stopping powers was further refined by removing approximations and using Brand Kitawa's theories on the degree of ionization of the ions.

2.1.2 Stopping power

The interaction forces that eventually make an ion stop when moving through an amorphous target, are usually expressed in terms of stopping powers [2]. They are determined by screened Coulomb interactions between the ion an the target atoms' nuclei and electrons [11]. The stopping power can be divided in two mechanism of energy loss that can be considered as independent in most applications [2], i.e. nuclear and electronic collisions. Therefore, the total stopping power is calculated as the sum of both [1]:

$$\frac{dE}{dx} = \left(\frac{dE}{dx}\right)_n + \left(\frac{dE}{dx}\right)_e \tag{2.1}$$

where x represents the ion penetration depth, E the ion energy and the subscripts n and e stand for nuclear and electronic stopping powers, respectively. Based on this concept,

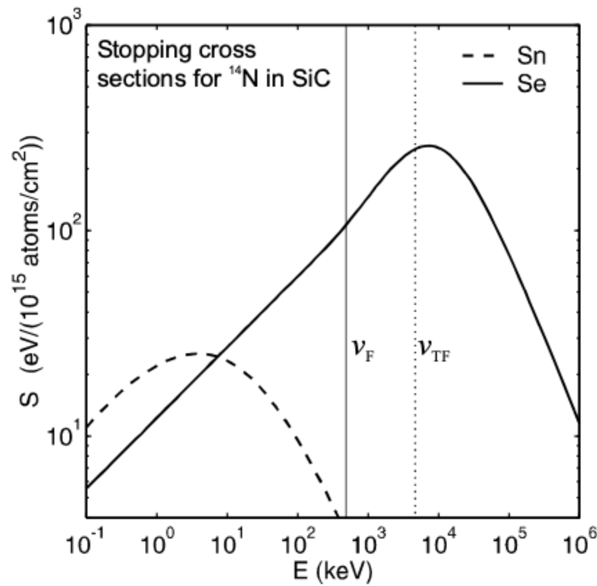

Fig. 2.1: Energy dependence of stopping cross-sections for ^{14}N in SiC. Nuclear cross-section, S_n, is represented by a broken line and electronic cross-section, S_e, by a solid line. The Fermi velocity v_F, and the Thomas-Fermi velocity v_{TF}, are shown as vertical solid and dotted lines, respectively [2].

the stopping cross-section can be computed as the energy-loss rate per scattering center

[11] with the following formula [1]:

$$S = \frac{1}{N}\frac{dE}{dx} = \frac{1}{N}\left[\left(\frac{dE}{dx}\right)_n + \left(\frac{dE}{dx}\right)_e\right] = (S_n + S_e) \tag{2.2}$$

where N is the target atomic density. From this definition, the range R of an implanted ion with initial energy E_0 can be calculated by integration [2]:

$$R = \frac{1}{N}\int_0^{E_0} \frac{dE}{S} \tag{2.3}$$

It is important to comprehend the differences between the mechanisms of ion stopping and be able to predict the weight of each of them depending on implantation conditions. Nuclear collisions refer to the elastic interactions between the impinging ion and the nuclei of the target atoms. They involve large energy losses per collision and considerable deflections, and inflict significant lattice disorder. They predominate at low energies and for implanted species with high atomic numbers Z_1 [11]. This mechanism will dominate at higher depths at the end of the implantation range, where the ion has lost most of its energy [1]. On the other hand, electronic stopping is based on the inelastic interaction between the implanted ion and the electron cloud of a target atom. [12]. Electronic stopping leads to lower energy loss per collision and negligible deflection angles, therefore they do not induce noticeable lattice disorder. This is the principal stopping mechanism at high energies and increases when implanting ions with lower atomic number, Z_1 [11]. The weight of both stopping cross-sections as a function of energy is visible in Fig. 2.1. These values also depend on other properties of implanted species and target material [2].

2.1.3 Nuclear stopping

Nuclear stopping involves elastic collisions between the implanted ions and the nuclei of target atoms, and is based on the transfer of kinetic energy between them. The study of this stopping mechanism can be approached from different perspectives. Complex molecular dynamics (MD) simulations study the energy transfer by evaluating the interaction between an ion and all the atoms present in a system as a function of time [2]. Since this method turns out to be highly time consuming, it is common to adopt a simplification that only considers the collision between two particles at a time. This is known as the binary collision approximation (BCA) and, according to it, the energy transfer is evaluated between an energetic moving ion and a stationary target atom. In this model, a moving particle M_1 with initial velocity v_o passes near a stationary atom M_2, whose relative position with respect to the M_1 trajectory is defined by the so-called impact parameter p. M_2 will absorb part of M_1 energy, recoiling at a velocity v_2 with a deflection angle φ with respect to the initial trajectory of M_1 . On the other hand,

the moving particle will also undergo a change in its trajectory and velocity, moving away at a velocity v_1 and with a deviation θ [2] (see Fig. 2.2). The final velocities and trajectories can be calculated from the conservation of momentum and energy of the system [10].

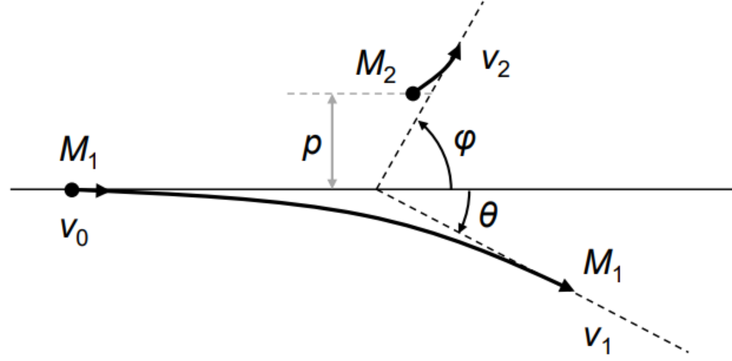

Fig. 2.2: Geometry of a two-body collision between a moving particle M_1 and a stationary one M_2 following the principle of binary collision approximation (BCA) [13].

These interactions are based on Coulomb forces between both particles. The repulsive potential at a given distance r can be calculated making use of Ziegler et al. universal interatomic potential [10], [13]:

$$V(r) = \frac{Z_1 Z_2 e^2}{r} \phi\left(\frac{r}{a}\right) \tag{2.4}$$

where Z_i are both particles' atomic numbers, e is the elementary charge, and the function $\phi(r/a)$ represents the screening function, which depends on the interatomic distance a, defined by Ziegler et al. as the universal interatomic distance, a_u [10]:

$$a_u = \frac{0.8854 a_0}{\left(Z_1^{0.23} + Z_2^{0.23}\right)} \tag{2.5}$$

a_0 is Bohr's radius, i.e. 0.529 Å. For the screening function Ziegler proposes Eq. 2.6 [10], although the formula can vary depending on the author.

$$\phi_u = 0.18175 e^{-3.1998 \frac{r}{a_u}} + 0.50986 e^{-0.94229 \frac{r}{a_u}} + 0.28022 e^{-0.4029 \frac{r}{a_u}} + 0.028171 e^{-0.20162 \frac{r}{a_u}} \tag{2.6}$$

From conservation of energy and momentum it is possible to calculate the energy transfer that takes place during the collision, i.e. the energy that the stationary atom

absorbs from the incident ion [2], [10]:

$$T_n = \frac{4M_1M_2}{(M_1+M_2)^2}E_0\cos^2\varphi, \tag{2.7}$$

referring to laboratory coordinates, where E_0 corresponds to the ion initial energy. Finally, the nuclear stopping power can be obtained from integrating the energy transfer of each collision T_n over all impact parameters, giving:

$$S_n = \int_0^\infty T_n 2\pi p dp. \tag{2.8}$$

Nuclear cross-section can be represented in terms of the reduced energy ε , a concept defined by Lindhard et al. [14] as:

$$\varepsilon = \frac{a_u M_2 E_0}{Z_1 Z_2 e^2 (M_1+M_2)} \tag{2.9}$$

.

The reduced energy was calculated by Ziegler et al. [10] as follows:

$$\varepsilon = \frac{32.53 M_2 E_0}{Z_1 Z_2 (M_1+M_2)\left(Z_1^{0.23}+Z_2^{0.23}\right)} \tag{2.10}$$

Numerical solutions for different values of ε were calculated and a function was fitted to represent the reduced nuclear cross-section [10]:

$$S_n(\varepsilon) = \frac{\ln(1+1.1383\varepsilon)}{2\left[\varepsilon+0.1321\varepsilon^{0.21226}+0.19593\varepsilon^{0.5}\right]},\ for\ \varepsilon \le 30 \tag{2.11}$$

$$S_n(\varepsilon) = \frac{\ln(\varepsilon)}{2\varepsilon},\ for\ \varepsilon > 30 \tag{2.12}$$

However, for practical calculations, the nuclear stopping of an incident ion with energy E_0 can be calculated as [10]:

$$S_n(E_0) = \frac{8.462\times10^{-15} Z_1 Z_2 M_1 S_n(\varepsilon)}{(M_1+M_2)\left(Z_1^{0.23}+Z_2^{0.23}\right)}\ \ eV/(atom/cm^2) \tag{2.13}$$

At lower velocities, the atom moves away from the ion at an early stage of the collision. As the ion energy E_0 increases, atom and ion get closer, which results in a higher potential in the collision. This implies larger energy transfer and, thus, greater nuclear stopping S_n. However, at certain point, the interaction time becomes the limiting factor in the collision, i.e. the stopping power decreases with incident energy [2]. This relationship of nuclear stopping with velocity, and therefore energy, can be

observed in the graph of Fig. 2.1.

2.1.4 Electronic stopping

Electronic stopping is one of the two mechanisms involved in the slowing down of an incident ion in a target material and it is related with high implantation energies and low Z_1. In comparison to nuclear stopping, these collisions cause smaller energy loss, deflection angles and lattice damage [11]. This type of stopping involves inelastic collisions and it is characterized by the excitation of the electrons of the ion or target atom. It can be understood as the coulombic interaction between the impinging ion and the electron cloud of an atom. The electronic stopping power is derived from different models depending on the velocity (and therefore, energy) regime of the ion (see Fig. 2.1).

Firstly, in the low energy regime, the ion has an incident velocity v lower than the Thomas-Fermi velocity v_{TF}, with $v_{TF} = v_0 Z_1^{2/3}$. v_0 is equal to Bohr's velocity, i.e. 2.19×10^8 cm/s or 25 keV/amu [2]. In this regime, the ion moves at lower speeds than that of the target's valence electrons, i.e. Fermi velocity v_F, and the collisions happen without direct energy loss [10]. The ion does not have enough energy to excite the electrons in the lower energy levels, thus only the ones close to the Fermi level contribute to the stopping [15]. Here, Firsov's theory can be applied. He stated that, since the two atoms have a relative velocity, there is some energy loss ΔE^F caused by the momentum needed to accelerate the captured electrons to the projectile velocity [10], [16] and can be calculated as a function of the impact parameter, p [2]:

$$\Delta E^F = \frac{0.35 m_e e^2}{\hbar} \frac{(Z_1 + Z_2)^{5/3}}{\left[1 + 0.16\,(Z_1 + Z_2)^{1/3}\, p/a_0\right]^5} v, \tag{2.14}$$

where m_e is the electron mass and a_0 is the Bohr radius, defined as $\hbar^2/m_e e^2 \approx 0.529$Å, being $\hbar$ the reduced Planck constant. Together with Firsov's geometric model, Lindhard and Scharf developed a similar theory, yet considering a more dynamic interaction between a slow heavy ion and a uniform electron gas [10]. The mean stopping cross-section, S_e is given by:

$$S_e^{LS} = \frac{8\pi\hbar^3}{m_e e^2} \frac{Z_1^{7/6} Z_2}{\left(Z_1^{2/3} + Z_2^{2/3}\right)^{3/2}} v \tag{2.15}$$

As it can be deduced from Eqs. 2.14 and 2.15, both models predict a proportionality relation between the electronic cross-section and the ion velocity. This approach presents some limitations, e.g. the lack of effects caused by the shell structure of the atom, which result in S_e oscillations with both Z_1 and Z_2 [17], while the Firsov and Lindhard and Scharf models predict a monotonic dependence. Other *ab initio* calculations have been

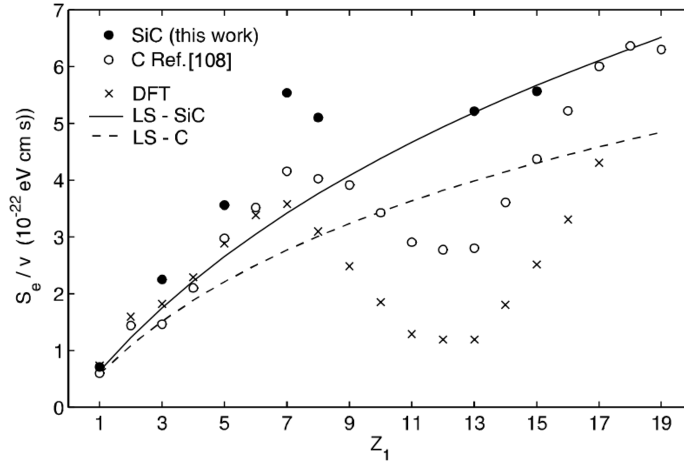

Fig. 2.3: Ratio of electronic stopping and ion velocity S_e/v as a function of Z_1 for SiC (•) and C (∘), obtained from experimental data. S_e/v predicted by Lindhard and Scharf (LS) theory is shown with a solid line in the case of SiC, and a broken line in the case of C. Also, calculations with Density Functional Theory (DTF) can be seen in the graph (×) [2].

developed using Density Functional Theory (DFT), in which electronic stopping power dependence with Z_1 arose [2]. This non-monotonic relation is depicted in Fig. 2.3.

On the other hand, different phenomena takes place at higher velocities. When the ion moves faster than v_{TF}, i.e. $v >> v_0 Z_1^{2/3}$, it can be assumed that it is fully stripped of its electrons and moves through the target as a bare nucleus [2]. At this point, where the velocity of the projectile is greater than that of the target electrons, the interaction between them is considered as the fast-collision case, and it can be regarded as a sudden, small external perturbation on the atom [11]. In this energy range, as v increases, the interaction time between the ion and the electrons diminishes, therefore decreasing S_e [11]. This behaviour is modelled according to the theory of Bethe and Bloch,

$$S_e^{BB} = \frac{4\pi Z_1^2 e^4}{m_e v^2} Z_2 L_S, \tag{2.16}$$

where L_S stands for the stopping number. Above the Bohr's limit, where $v > 2Z_1 v_0$, L_S is given by Bethe theory as $L_{Bethe} = ln(2m_e v^2/I_e)$ [18]. Here, I_e represents the mean ionization energy of the target electrons and it is approximated by Bloch as $I_e \approx 10Z_2\ eV$ [12]. At intermediate velocities around $v \approx v_0 Z_1^{2/3}$ the study of the electronic stopping becomes complex due to the partial stripping of the ion. In this region S_e reaches its maximum above v_{TF}, when the ion velocity is similar to that of

the outer electrons and the time that the ion spends in the vicinity of the atom is the highest possible [12].

2.2 Ion channeling

The study of the stopping powers as it was presented in the previous sections will only be well grounded if the stopping medium, i.e. the implantation target, is amorphous [11]. However, implantation is often performed in crystalline materials, where rows of atoms are arranged in high-symmetry planes or directions and form channels. When an ion is impinged into a crystalline target, it can be injected into one of this channels. It will be directed to its center and will undergo small angle collisions that result in an oscillating movement (see Fig. 2.4), due to the fact that the channel walls form an approximately continuous potential [2]. Since the ion is confined in the center of the

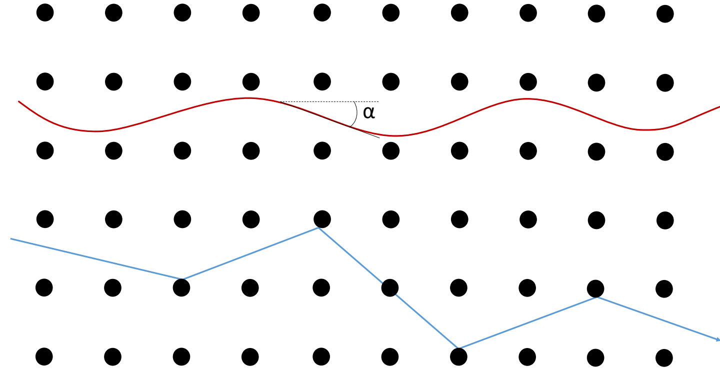

Fig. 2.4: Sketch of a random ion trajectory (blue) and a channeled ion (red) in a crystalline structure.

channels, close encounters are avoided and therefore, so is the nuclear stopping power. Moreover, electronic stopping also decreases, considering that the electron density is lower in these regions [2]. This results in higher ranges for channeled ions in comparison to the depth achieved by those following a random trajectory.

However, a channeled ion can also be ejected, which is the case of ion dechanneling. This phenomenon will take place when the transverse component of the ion kinetic energy $E_\perp$ is higher than the potential energy of the channel wall, with $E_\perp$ [19]:

$$E_\perp = \frac{1}{2} m v_\perp^2 \tag{2.17}$$

where m is the ion mass and $v_\perp$, the component of the ion velocity perpendicular to

the direction of the channels. This velocity can be expressed as:

$$v_{\perp} = v_0 \sin \alpha \tag{2.18}$$

where v_0 represents the initial velocity of the impinging ion and α is the angle between the instantaneous trajectory of the ion and the direction of the channel wall [2]. Therefore, the transverse component of the ion's kinetic energy can be expressed as:

$$E_{\perp} = \frac{1}{2} m v_{\perp}^2 = \frac{1}{2} m v_0^2 \sin^2 \alpha = E_0 \sin^2 \alpha \tag{2.19}$$

For small angles $\sin \alpha \approx \alpha$, and therefore:

$$E_{\perp} \approx E_0 \alpha^2 \tag{2.20}$$

In its oscillating movement, the ion will approximate to the channel walls. The minimum distance to the row of atoms at which the ion can still remain channeled is known as the critical distance r_{crit}, which allows the definition of the critical angle α_c. Provided that the potential of the wall at this distance, $V(r_{crit})$ is known [19], the critical angle is calculated as:

$$\alpha_c = \sqrt{V\left(r_{crit}\right)/E_0} \tag{2.21}$$

If an ion achieves a transverse kinetic energy sufficiently high, such that its trajectory exceeds this critical angle, it will be dechanneled. The energy at which this angle is achieved is the critical transverse energy, $E_{\perp crit}$.

The probability that dechanneling happens is tightly related to the effect of thermal vibrations, which increase transverse energy at the same time that limit $E_{\perp crit}$ [2]. Dechanneling is also enhanced by defects on the lattice, particularly by interstitial

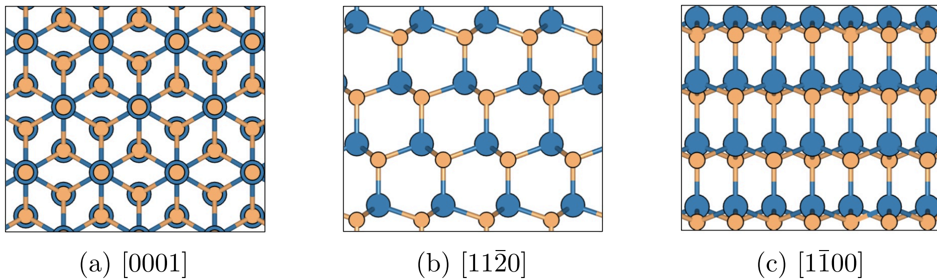

(a) [0001] (b) [11$\bar{2}$0] (c) [1$\bar{1}$00]

Fig. 2.5: Crystallographic structure for some of the preferred directions for ion channeling in 4H-SiC. Si atoms are represented in blue, while C atoms are orange [13].

defects [2]. Moreover, channeling is, in the first place, constrained by different factors, e.g. the implantation direction. For titled implantations, this symmetry directions are usually avoided and ranges are lower since the ions move randomly through the target.

Ion channeling also depends on the planar atomic density of the particular directions and the opening of the channels (see Fig. 2.5). For directions with higher planar atomic density, the fraction of channeled ions is smaller. Furthermore, directions which present channels with wider openings give lower electronic stopping and result in higher ion ranges [2]. Another factor that governs channeling is the position of the incident ion in the plane perpendicular to the channel direction, as shown in Fig. 2.6. Ions going into the sample close to an atomic row will probably not become channeled. Those being implanted further away from the channel walls are more likely to be injected into these paths, but will undergo larger oscillations than those which entered near to their center and have a better chance of remaining channeled through the stopping process [11].

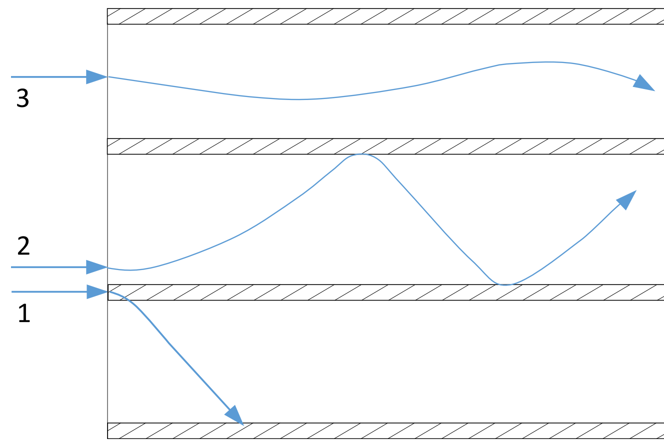

Fig. 2.6: Dependence of ion channeling on the position of the incident ion in the plane perpendicular to the channel. Typical trajectories for ions implanted into an atom wall (1), close to it (2) and into the center of the channels (3), are depicted.

However, ion channeling does not depend entirely on the above mentioned implantation conditions. An ion can be channeled by means of scattering throughout all the stopping process. Ultimately, channeling makes the study of ion ranges more complex and unpredictable. On the other hand, it presents other advantages like the decrease of implantation-induced damage, since close collisions are avoided and, thus, so is nuclear stopping, which is the primary cause of lattice disorder. Furthermore, channeling is a potential alternative to achieve deeper junctions, due to the increased ranges that result from the reduced stopping powers [11].

2.3 Implantation-induced damage

Low diffusion coefficients of SiC and the need for strict control over the introduced impurities in the samples result in the substitution of in-diffusion by ion implantation as the preferred doping technique for this semiconductor [10]. However, this method is closely related to the emergence of lattice damage. During ion bombardment, target atoms gradually receive kinetic energy from the incident ions and can eventually be displaced from their position. While the main cause of implantation-induced damage is found in elastic collisions, inelastic collisions, i.e. electronic interactions, intensify the diffusion of defects and can lead to their migration and cluster [10]. The characteristics of the induced damage depend on the energy T transferred in these interactions. The energy necessary to move a target atom out of its lattice position is known as displacement energy, E_d. If an energetic ion gives away an amount of energy lower than E_d, i.e. $T < E_d$, the target atom will oscillate within its position, dissipating the remaining energy as heat. Conversely, if $E_d < T < 2E_d$, the atom will get knocked-out of its position, which then is occupied by the incident particle. Either a replacement collision or an interstitial will take place, depending on whether incident and displaced particles are the same species or not, respectively. Lastly, if $T > 2E_d$, both the ion and the knocked atom will still have enough energy to recoil away and potentially displace other atoms in the lattice. In this situation a Frenkel pair is formed, i.e. an interstitial and a vacancy [1], [11]. Besides these point defects, linear, planar and volume defects can also take place [11]. Moreover, they may form complexes when combined or joined with impurities in the substrate [3] during the thermalisation process and formation of the damage cascade, which is a result of the subsequent displacement of the atoms throughout the implantation process.

To have a good understanding of the state of the host material after implantation, one needs to consider the influence of different parameters in this phenomenon. The mass of the implanted ion will impact the number of Frenkel pairs, while the energy with which they are shot towards the substrate will affect their distribution. Damage profiles with distinct size and density can be achieved by adjusting these two parameters. Other variables complete the definition of the damage obtained after implantation, e.g. temperature characterizes the way defects form, migrate and dissociate [2].

The study of the formation of implantation-induced damage is usually addressed following the damage cascade model. It refers to the atoms displaced from their lattice site by an incident ion as primary knocked-on atoms (PKA) [11]. When they move through the substrate they can eventually displace other atoms, which will be referred to as secondary knocked-on atoms. Analogously, tertiary, quaternary, etc. atoms will form their corresponding amount of damage. This results in the formation of a damage cascade (see Fig. 2.7). The dose dependence plays, again, a decisive role. For higher doses, the probability of different cascades to overlap is enhanced, which could even lead to amorphisation of the substrate [2]. A simplified way to calculate the number of

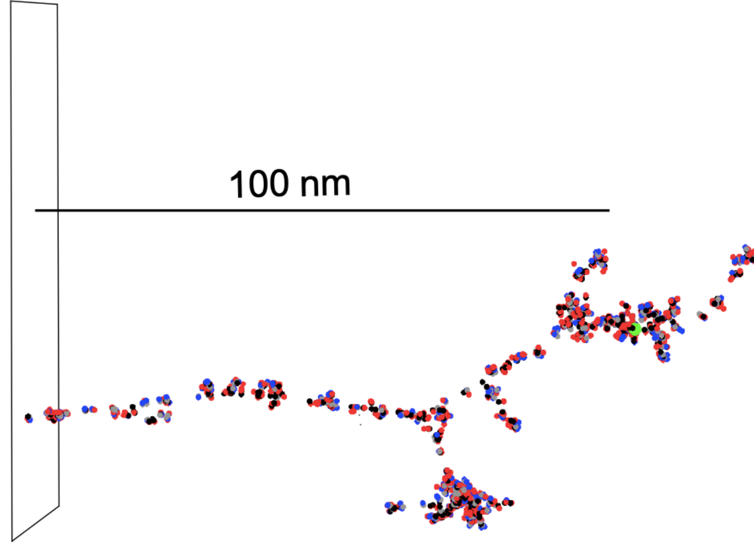

Fig. 2.7: MC-BCA simulation of the damage cascade created by a single 100 keV Al (●) ion implanted in 4H-SiC. C and Si interstitials are represented as (●) and (●) respectively, while C and Si vacancies are shown as (●) and (●) [2].

displaced atoms is the modified model of the Kinchin and Pease proposal as shown in Eq. 2.22 [20] [21]:

$$N_d = \begin{cases} 0 \; for \; T_n < Ed \\ 1 \; for \; E_d \leq T_n < \dfrac{2 \cdot E_d}{0.8} \\ \\ \dfrac{0.8 \cdot T_n}{2 \cdot Ed} \; for \; T_n \geq \dfrac{2 \cdot E_d}{0.8} \end{cases} \tag{2.22}$$

where T_n is the energy transferred in nuclear collisions.

The comprehension of implantation-induced damage becomes a matter of high interest, considering that it can modify electrical and mechanical properties of the semiconductor. It also deteriorates the roughness of the surface, which can lead to the decrease of impurity concentration after annealing [1]. Moreover, this phenomenon gives information about the the energy transfer in elastic collisions and perturbs the movement of ions and displaced atoms through the substrate. Dechanneling rates are greatly enhanced by implantation-induced damage, particularly for the high dose and high energy range, where the channels become saturated by knocked-on atoms [2]. Therefore, efforts are

made in order to avoid lattice disorder by means of a combination of high temperature implantation and post-implantation annealing (usually around $1600 - 1700$ °C [2]). The adjustment of tilt angles in order to achieve channeling directions is also being explored as a possibility to reach deep implantation with lesser amount of damage [11].

Chapter 3

Simulation of Ion Implantation

In order to achieve the manufacturing of power electronics devices with a competitive cost, time and material resources need to be optimized. Therefore, simulation algorithms that predict depth profiles with a high degree of accuracy and low computational costs are a prime priority.

There are two main approaches to analyse the depth profiles of implanted ions. One of them is the analytical method, which describes the ion ranges by fitting the profiles to a certain statistical function, characterised by its distribution moments, e.g. mean or standard deviation. Some of the typical functions used for SiC are the Gaussian, Pearson IV and dual Pearson. A different approach to study implantation depth profiles is developing simulators that are based on the physical phenomena that rule ion stopping. While statistical models offer instant execution times, they are tightly constrained by implantation conditions and require of large amounts of experimental data. This problem can be avoided following the physical approach, which is more accurate and flexible. However, its computational costs become a limiting factor, and a compromise between accuracy and execution time needs to be met.

Overall, these algorithms predict depth profiles with an acceptable degree of accuracy, yet they present several limitations in particular cases. The understanding of ion behaviour in the high energy range remains a challenge and it is decisive to achieve the effective simulation of power electronic devices that need of deep implantation, e.g. superjunction MOSFETs. The characteristics of several simulation alternatives are evaluated in this chapter in order to find the best suited solution for high energy ion implantation in 4H-SiC.

3.1 Statistical models

Statistical simulators of ion implantation describe the final concentration distribution in the target as a particular probability function. The depth profiles are extracted from the distribution moments and, since these models do not study the complex interaction between the energetic ions and the target atoms, the execution is almost instantaneous. In order to obtain the distribution moments and eventually represent a particular depth profile, large amounts of data need to be gathered. This is accomplished either by

carrying out experiments and measuring the results, or by running more sophisticated simulations and treating the outcome as experimental data. The information will be analysed and either tabulated for future interpolation, or fitted to obtain the expressions of the distribution moments as a function of certain parameters, usually implantation energy, dose and ion species. However, the results also depend on other factors such as temperature, energy range or tilt angle. That is why statistical simulators are tightly constrained by the conditions at which the experimental data was obtained and why these models are limited in terms of flexibility.

3.1.1 Pearson IV distribution

Following an analytical approach, implantation depth profiles can be fitted to statistical distributions. Finding the one which adjusts to the profiles in a finer way is one of the main challenges. Ashworth et al. concluded that the Pearson family, including the Gaussian, are adequate for this purpose. Among them, the superiority of one distribution with respect to other depends mainly on the implantation conditions [22]. In the case of ion implantation in SiC the Pearson IV appears to give satisfactory results. The fact that this distribution has no negative values and presents a single maximum makes it advantageous compared to other distributions like the joined half-Gaussian and the Edgeworth distributions [23]. Moreover, lateral straggling and implantation tails, which make depth profiles deviate from the Gaussian distribution, can be slightly improved with the Pearson IV [1].

The Pearson IV distribution is described through the first four moments, which are: (1) Mean, which in our case will measure the mean projected range Rp, (2) Standard deviation ΔR_p, (3) Skewness γ, which represents how asymmetric or shifted the profile is with respect to the normal distribution and (4) Kurtosis β, which describes how sharp the distribution is around the tipping point [24]. They are defined as follows [8]:

$$R_p = \frac{1}{I} \int_{-\infty}^{\infty} x f dx, \quad I = \int_{-\infty}^{\infty} f dx \tag{3.1}$$

$$\Delta R_p = \sqrt{\frac{1}{I} \int_{-\infty}^{\infty} (x - R_p)^2 f dx} \tag{3.2}$$

$$\gamma = \frac{1}{I \Delta R_p^3} \int_{-\infty}^{\infty} (x - R_p)^3 f dx \tag{3.3}$$

$$\beta = \frac{1}{I \Delta R_p^4} \int_{-\infty}^{\infty} (x - R_p)^4 f dx \tag{3.4}$$

The differential equation of the Pearson distribution is defined as [1]:

$$\frac{df(x)}{dx} = \frac{(x-a)f(x)}{B_0 + B_1 x + B_2 x^2}, \tag{3.5}$$

and depends on $\eta = B_1^2 - 4B_0B_2$. For the Pearson IV, where $0 < \eta < 1$, this equation gives the following formula [8]:

$$P_{IV} = \frac{1}{M}\exp\left[-n\arctan\left(\frac{x-R_p}{A} - \frac{n}{r}\right)\right] \times \left[1 + \left(\frac{x-R_p}{A} - \frac{n}{r}\right)^2\right]^{-m} \tag{3.6}$$

$$r = -(2 + 1/B_2), \quad n = -ra\left(4B_0B_2 - a^2\right)^{-1/2}$$

$$m = -1/2B_2, \quad A = mra/n$$

$$a = -\Delta R_p \gamma (\beta + 3) C, \quad B_0 = -\Delta R_p^2 \left(4\beta - 3\gamma^2\right) C$$

$$B_2 = -\left(2\beta - 3\gamma^2 - 6\right) C, \quad C = \frac{1}{2(5\beta - 6\gamma^2 - 9)},$$

where M is a normalisation factor of the distribution [8].

In order to be able to describe the implantation profiles as a Pearson IV distribution, a fitting process is to be carried out. One needs to run a high number of experiments in the desired energy range. Of course, other parameters like the tilt angle, ion-target material combination, etc. have an influence on the final concentration profile. This lack of flexibility is one of the main limitations of statistical models. However it is commonly accepted so as to obtain a fairly generalised approach. Once a considerable amount of data is retrieved, the moments of the implanted profiles will be extracted and tabulated. When simulating at a certain implantation energy, the distribution moments for it will be obtained by means of interpolation of these tables. A different alternative consists on developing analytical functions of the distribution moments fitted to the data and then tabulate their fitting parameters. Janson et al. proposed a set of fitting factors and equations (eqs. 3.7) that calculated the distribution moments as a function of implantation energy and gave overall reasonable predictions [8].

$$R_p = a_1 E_r^{a_2} E_r^{a_3 \ln E_r} E_r^{-a_4 (\ln E_r)^2}, \quad (E_r = E/1keV), \tag{3.7}$$

$$\Delta R_p = \frac{b_1}{1 + (b_2/E)^{b3}},$$

$$\gamma = \left(c_1 - c_2\sqrt{E}\right)\exp\left(-\frac{E}{c_4}\right) - c_3\exp\left(-\frac{c_4}{E}\right),$$

$$\beta = \left(d_1 + 2.5e^{-d_2/E}\right)\beta_0,$$

$$\beta_0 = \frac{48 + 39\gamma^2 + 6\left(\gamma^2 + 4\right)^{1.5}}{32 - \gamma^2},$$

Here, a_i, b_i, c_i, and d_i, with $i = 1, ...$ are the fitting parameters obtained from experimental data. They can also be obtained by carrying out sophisticated simulations and treating the results as experimental. Janson et al. performed implantations of ^{1}H, ^{2}H, ^{7}Li, ^{11}B,^{14}N, ^{16}O, ^{27}Al, ^{31}P, ^{69}Ga, and ^{75}As in 4H-SiC (with some exceptions, that were implanted in 6H-SiC). The implantations were carried out in the 3.7 keV-3.2 MeV energy range and the other parameters were tuned in such a way that amorphization was avoided (for ^{27}Al implantations at 300 K this is usually given at doses below 1×10^{14} cm^{-2}). The ions were directed perpendicular to the sample's surface. This makes the implantation directions fixed by the off-axis cut of the samples, which in this case resulted to be 8° and 3.5° respectively for 4H-SiC and 6H-SiC. The final fitting factors for these cases are listed in Table 3.1:

Ion	a_1 (nm)	a_2	a_3 (10^{-3})	a_4 (10^{-3})	b_1 (nm)	b_2 (keV)	b_3	c_1	c_2 ($keV^{-1/2}$)	c_3	c_4 (keV)	d_1	d_2 (keV)
^1H	16.3	0.76	38.3	7.1	61	5.6	0.99	1.24	1.35	1.4	21	1.4	∞
^2H	16.4	0.85	38.9	8.1	105	11.4	0.96	0.26	0.44	1.3	151	1.5	241
^7Li	3.79	1.12	-27.8	0.3	120	43.4	1.07	1.26	0.44	0.1	245	1.5	10
^{11}B	1.39	1.53	-119	-5.7	124	116	0.76	-0.09	0.06	1.9	83	1.5	519
^{14}N	1.23	1.17	-26.0	0.6	147	297	0.84	-1.21	-0.04	2.8	109	1.5	269
^{16}O	3.47	0.62	72.6	6.5	120	108	1.07	1.62	0.32	0.9	692	1.5	15
^{27}Al	3.34	0.42	113.6	8.4	239	484	0.88	1.76	0.16	2.2	858	1.5	126
^{31}P	1.43	0.74	72.8	6.8	188	411	0.97	0.86	0.02	1.4	476	1.2	∞
^{69}Ga	5.60	0.01	122.2	4.1	774	3220	1.11	1.00	0.02	0.0	190	1.1	∞
^{75}As	0.84	1.15	-84.6	-7.3	1890	15200	0.87	3.60	0.08	0.7	392	1.1	∞

Tab. 3.1: Fitting parameters for Eqs. 3.7 by least squares from the experiments and simulations carried out by Janson et al. [8].

In Fig.3.1 one can observe that the profiles calculated from this fitting parameters remain consistent with SIMS measurements for a wide range of energies. However, some inconsistencies show up at the low concentration ranges in the tail of the distributions. This effect finds its explanation in the channeling of the implanted ions. This rather unpredictable phenomenon is predominant at low energies since the channeled ions have a higher probability of staying contained between the atom rows. Considering that the Pearson distribution does not take into account ion channeling, the larger deviations with respect to the real profiles around the deeper ranges can be explained.

From Janson et al. fitting parameters, an ion implantation simulator was developed in

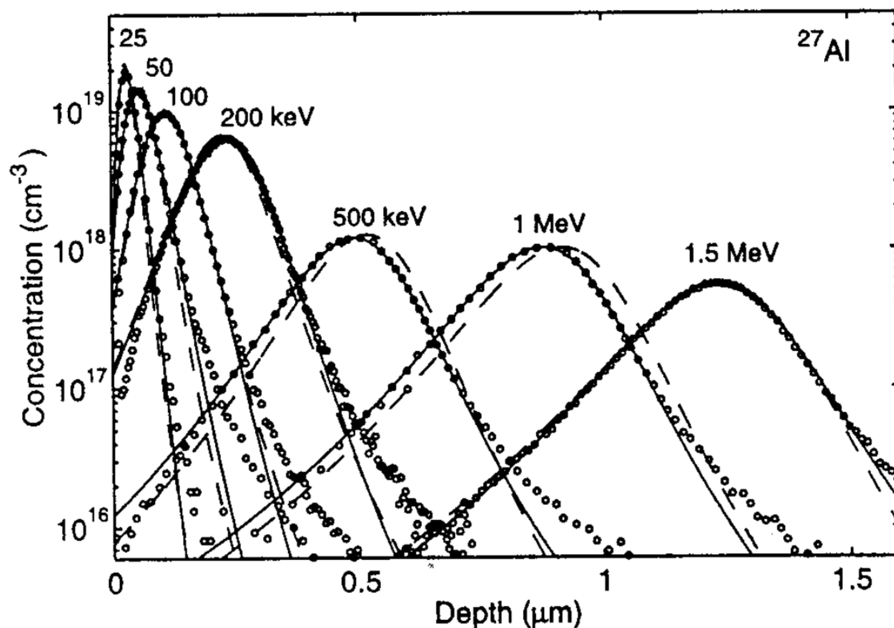

Fig. 3.1: Comparison of Al depth profiles obtained from SIMS measurements (∘), their linear fit to a Pearson function (solid lines) and the profiles calculated from Eqs. 3.7 with the fitting parameters given in Table 3.1 (broken lines) [8].

Matlab by Y. Ju [1]. This model will be used later on with the object of comparing the effectiveness of this simulation method with respect to other alternatives. This program, named *Implantor.m*, has instant execution times since it is based on a statistical model. However, the possibilities provided by it are limited, i.e. only uni-dimensional depth profiles can be computed. Implanted species (Al for p-doping and P for n-doping), dose and energy are chosen for every implantation, but other parameters such as tilt angle or temperature cannot be adjusted by the user.

3.1.2 Dual Pearson distribution

As it was demonstrated in the previous section, the Pearson IV distribution gives precise implantation profiles, yet this model breaks down when dealing with the tails of the profiles, both at the shallow and deep ranges, where the ion concentrations are low. This deviations stem from the differences between the trajectories of the impinging ions during the implantation process, which can be classified in three groups: ions randomly scattered through the sample, ions involved in collisions with large deflection angles that have a high probability of being backscattered and, lastly, ions trapped

between atom rows, whose interaction with lattice particles is reduced and, therefore, their movement ceases at deeper ranges, i.e. channeled ions [25]. In fact, channeling and backscattering effects are implicitly included in the empirical data upon which statistical models are built. However, if the distributions at issue are not flexible enough they will not be able to incorporate this effects [26], which have less significance than the ions moving randomly that represent the bigger fraction of the implantation dose and are deposited around the projected range R_p. Aiming to solve this issue, Tasch et al. proposed a model which consisted in the sum of two weighted Pearsons [27], which will be referred to as the dual Pearson distribution. The main goal of this approach is to take into account the low and high depth tails of the profiles caused by channeling and backscattering effects. The depth profile of the implantation is defined with the following expression:

$$N(x) = \phi\,[Rf_1 + (1-R)f_2], \tag{3.8}$$

where f_1 and f_2 represent both Pearson distributions, which can generally be considered as independent [26]. The former accounts for the core ions that undergo small deflections and constitute the high concentration areas around R_p. The latter, f_2, considers the smaller fraction of ions that can be considered as backscattered or channeled and form the low concentration tails of the profile. ϕ is the total implanted dose and R is the ratio between the randomly moving ions with respect to the total dose, which describes the weight of the core or "main" Pearson. This weight will increase with build-up damage and filling of the channeling tails in the case of higher energies or doses [28]. The ratio R allows to adjust this relationships in order to get more accurate results. Moreover, having two distributions improves the flexibility of the model which will adapt better to the characteristic asymmetries of implantation profiles.

In order to define a dual Pearson distribution nine parameters are needed: four per each Pearson (R_p, ΔR_p, γ and β) and the dose ratio R corresponding to the weight of f_1. This larger number of parameters will make the fitting process more complex than that for the Pearson IV. Reliable results have been obtained for the fitting of Si implantation profiles to the dual Pearson, yet in the case of 4H-SiC there is still scope for improvement [29]. Other issue that needs to be addressed is the fact that both Pearson distributions are considered independent. Although significant accuracy can be achieved adopting this principle, in reality, initially randomly scattered ions can become channeled and vice versa, i.e. channeled ions may be dechanneled as seen in Sec. 2.2. Dual Pearson profiles will usually underestimate the weight of the main Pearson (R) by ignoring the potential dechanneling [26] that may take place.

If the focus is set in the high energy range, the use of the dual Pearson is advantageous, due to the fact that in this region the profiles show more pronounced asymmetries, which would not be possible to represent for the single Pearson IV function. Nonetheless, the lack of extensive experimental data bases, together with the increased number of distribution moments necessary to define the function, make their fitting and modelling

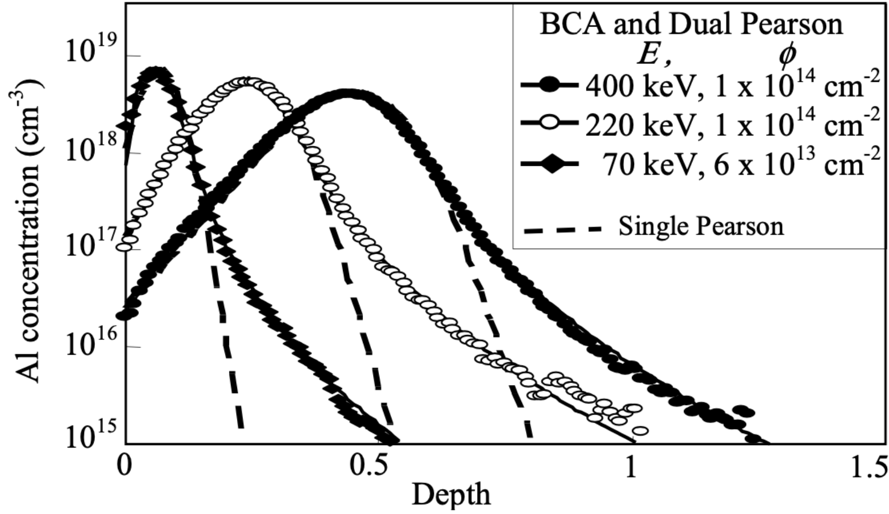

Fig. 3.2: Comparison between BCA simulations, Pearson IV and dual Pearson fittings to depth profiles of Al implantation in 4H-SiC [29].

rather difficult.

3.2 Physical models

A different approach to study implantation depth profiles is developing simulators that are based on the physical phenomena that rule ion stopping. These models are more accurate and flexible than statistical ones. However, their computational costs become a limiting factor, and a compromise between accuracy and execution time needs to be met. Physical models are, in turn, subdivided in simulators based on two different principles: molecular dynamics (MD) and the binary collision approximation (BCA). As it was introduced in Sec. 2.1.3, the first alternative, i.e. MD, provides results that adjust more precisely to the real profiles, yet the computational cost is higher. On the other hand, BCA, whose schematic working principle was depicted in Fig. 2.2, improves the execution time by compromising the accuracy of the results. Despite these potential deviations with real implantation profiles, the results are generally satisfactory. Hence, simulators rooted on the BCA are the most widely used alternative at the moment. They are based on the Monte-Carlo method, i.e. the final profile is formed by addition of individual ion trajectories, affected by a set of random parameters [2].

The critical issues of MC-BCA, for taking a significant part of the total execution time, are algorithms used to find the next collision partner and the way to solve the scattering integral [2]. Due to the large number of interactions and iterations needed

to achieve a reliable profile, an efficient technique for the search of the atoms that will interact with the ion during the event-driven simulations will result in a major improvement on the overall efficiency of the program by saving valuable computation time. The trade-off between accuracy and computational costs is, once again, faced when deciding how is the scattering integral going to be solved, i.e. with complex but accurate numerical methods or by using an approximating analytical expression, i.e. Biersack's *Magic Formula*. Moreover, other aspects need to be taken into account to evaluate the performance of these simulators. The presence of thermal vibrations, which will enhance the dechanneling rate and could affect the search for the collision partners, is an issue worth studying. The same applies for the need of including the dose dependence: for higher doses, with the saturation of the channels and damage accumulation, dechanneling is likely to occur, which has a direct impact on the range profiles of the implantation. In relation to this, the model adopted for describing the implantation-induced damage is significant. Both the full damage cascade and the simplified Kinchin Pease models are widely included into implantation simulators. The full damage cascade model studies the trajectory and cascades formed by secondary and subsequent displaced atoms once the primary knocked-on atom trajectory is completed. This is possible due to the fact that there is no time dependence between collisions, i.e. they are event-driven. On the other hand, as it was explained in Sec. 2.3, the Kinchin Pease approach calculates the damage function as proportional to the energy transferred in the elastic collisions. Simulators based on physical models generally feature both alternatives. While the Kinchin Pease avoids simulating every trajectory, therefore making the calculation of damage faster and simpler, it provides less precise results. The alternatives available today give a particular treatment to all of this issues and present different characteristics because of it. Understanding their behaviour, as well as their limitations and advantages, is crucial when deciding which simulator will be used.

3.2.1 SIIMPL: Simulation of Ion Implantation

This algorithm, which was developed by Martin Janson [30], initially aimed to attain a precise and efficient way to simulate the outcome of ion implantation in SiC. However, it can also be used to study implantation results in a wide range of substrate materials, both crystal and amorphous targets. The principle followed by this program is based on MC-BCA. The basic concepts behind this event-driven approximation are depicted in Fig. 3.3. When an ion is injected into the sample it will undergo interactions with some of the lattice atoms, referred to as A, B and C in Fig. 3.3. The collision partner for the ion is the atom which is closest to the ion (measuring the projected distance over the ion trajectory) in the direction of the movement. Moreover, in order to be eligible as collision partner, the atom needs to have an impact parameter p no greater than a maximum value p_{max}. In the schematic image, since C is further than p_{max}, the first collision partner to the incoming ion will be A. When the ion reaches I', its trajectory

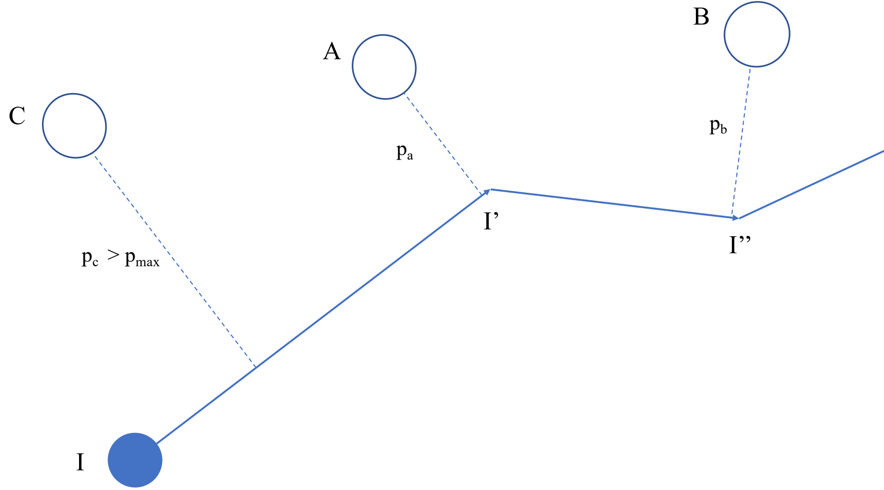

Fig. 3.3: Schematic representation of consecutive binary collisions between an ion I and target atoms A and B.

will be deflected. Then, B, the next atom with which it will interact in I'', deviates its movement again. This subsequent collisions will continue until the ion energy is lower than a threshold, below which the ion can be considered as stopped [2].

As stated above, one of the critical points of Monte-Carlo based simulators is finding an efficient way to search for the next collision partner. The goal is to reduce the number of evaluations of potential interaction atoms maintaining, at the same time, an acceptable level of accuracy. For efficiency reasons, SIIMPL uses an algorithm which divides the substrate in cells and subsequent sub cells. In the study of the particle's interactions, the sub cell containing the energetic ion will be identified first. Hereafter, the next collision partner will be searched among the atoms belonging to a confined volume. This volume is defined by the sub cell itself, together with an additional volume containing the atoms which are no further away than p_{max} from the sub cell walls [30]. With this approach the search volume is reduced, therefore improving the computational cost of one of the most time-demanding procedures of ion implantation simulations. The way of solving the scattering integral, which defines how the particles recoil away after colliding, is another crucial issue when simulating ion implantation. It can be addressed by numerical integration of Eq. 3.9.

$$\varphi = \int_{r_0}^{\infty} \frac{pdr}{r^2 g^{1/2}}, \qquad g = 1 - \frac{V(r)}{E_c} - \left(\frac{p}{r}\right)^2 \tag{3.9}$$

$$E_c = \frac{E}{1 + \frac{M_1}{M_2}},$$

where r_0 represents the apsis of collision, i.e. the smallest distance between particles throughout the collision, and is obtained from $g(r_0) = 0$ [2]. In order to improve execution times, an approximate analytical formula can be used, namely the *Magic Formula* developed by Biersack et al. This approach is the default option selected in SIIMPL and gives fairly accurate results.

Furthermore, the treatment given to the electronic collisions is decisive. SIIMPL subtracts the corresponding energy loss after each collision, taking into account the local and non-local stopping forces [30]:

$$\Delta E = S_e \left[(1 - f_1)\, N \Delta r + f_1 A \exp(-sp\,/a_U)\right] \tag{3.10}$$

$$A = s^2/(2\pi a_U^2[1 - (1 + sp_{max}/a_U)\exp(-sp_{max}\,/a_U)])$$

where f_1 is a weighing factor between 0 and 1. s is a fitting parameter, which influences the magnitude of electronic stopping for channeled particles and, consequently, the depth that they reach after being implanted [30]. The electronic stopping cross section S_e can be calculated by interpolation of the results that Lindhard-Scharff and Ziegler formulas give for low and high velocity stopping, respectively. The interpolation will be calculated following the proposal of Biersack and Haggmark:

$$S_e = \left(\frac{1}{S_e^{lo}} + \frac{1}{S_e^{hi}}\right)^{-1} \tag{3.11}$$

Moreover, the electronic stopping can also be imported from SRIM 2003, a well-known

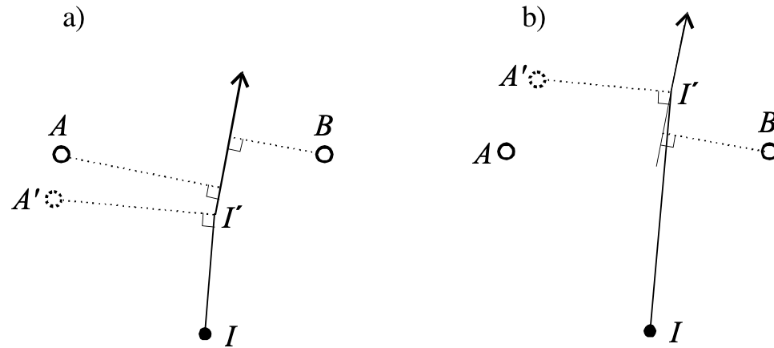

Fig. 3.4: Representation of the effect of thermal vibrations in the lattice atoms by displacing them a)closer or b)further away from the incoming ion [2].

program developed by Ziegler et al., more efficient than SIIMPL.

Additionally, the SIIMPL algorithm is characterised by the way that the effect of thermal vibrations is included. Other algorithms proceed in such a way that the collision partner is found first. Once the collision partner is identified, the thermal vibrations are added. Displacements caused by these vibrations can bring the atoms closer or further away from the ion (see Fig.3.4). In the second situation, there might be the case that the ion does not collide with the initial partner after all. This problem leads to an overestimation of the dechanneling effect by these algorithms. However, SIIMPL deals with this issue by adding the effect of the thermal vibrations before searching for the collision partner. It is accomplished by treating thermal vibrations as an oscillating function that depends merely on the lattice position r. The comparison between both treatments can be appreciated in Fig. 3.5. The implantation depth profiles were

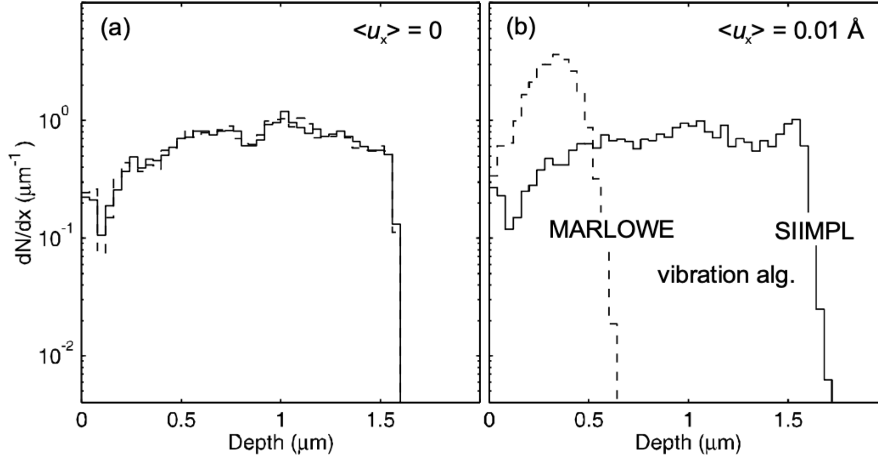

Fig. 3.5: Depth profiles given by MARLOWE (broken lines) and SIIMPL (solid lines) algorithms for a 100 keV X implantation into the $< 001 >$ direction for a single cubic target. On the left the simulation was performed without including thermal vibrations. On the right, displacements of 0.01Å are added [2].

obtained both for a frozen lattice and including the effect of very low thermal vibrations (0.01 Å). The lower depths given by the algorithm where the thermal vibrations are added after searching for the collision partner (i.e. the MARLOWE algorithm) reveal the overestimation of the collisions, since such small displacement must give a profile closer to that of the frozen lattice simulation. This is precisely the case of the results

obtained from SIIMPL.

On the other hand, it is important to appropriately decide the damage model that is going to be used. Although SIIMPL uses the Kinchin Pease model by default, it offers the possibility of employing the full damage cascade model in order to obtain more precise results, especially in those cases were the damage distribution is the main interest. Moreover, this algorithm takes into account the very important dose dependence, which is particularly evident at higher doses when the damage has accumulated at the tail of the channels. SIIMPL calculates the probability of each collision to be with an interstitial and then a random number determines if the ion will impact with an interstitial or lattice atom.

In order to improve the algorithm efficiency and computational cost while maintaining a good representation of the channeling effect, SIIMPL includes the rare depth or rare event algorithm. A rare depth can be understood as a depth, past which the ions can be considered as channeled. A set of rare depths are determined, and when an ion reaches this point it is replicated in pseudoions, whose trajectory will just be evaluated from this depth on. In this way, the number of iterations needed to achieve an accurate representation of this rare event, i.e. channeling, is considerably reduced. These and other functions make of SIIMPL an appropriate algorithm to study ion implantation in 4H-SiC.

3.2.2 SRIM: Stopping and Range of Ions in Mater

Around the 80's, J. F. Ziegler, J.P. Biersack and M. D. Ziegler developed their intensive work regarding the stopping and range of ions in mater in the different states (i.e. solid, liquid and gas). Their research focused on the behaviour of incoming ions in matter. The main issues treated are the stopping powers that govern the ion movement, together with the final distribution that they adopt after the implantation process. With this objective, a set of experimental data are provided, in addition to thorough theoretical explanations. Moreover, their work also aims to attain a better understanding of implantation-induced defects. To complement these studies, a group of programs were developed, namely SRIM (which, again, stands for Stopping and Range of Ions in Matter). Among these, one particular program stands out. It is the so-called TRIM (Transport of Ions in Matter). Through a user-friendly interface it allows the simulation of ion implantation in a wide range of amorphous materials [31].

The main attraction of SRIM is that it finds a good compromise between accuracy and computational costs. This is mainly achieved through two mechanisms. On the one hand, the scattering integral is solved analytically with the *Magic Formula*, which was already introduced in previous sections, and allows a faster resolution of the collisions. On the other hand, one of the main reason of high execution times is the large number of interactions that a moving particle undergoes until being fully stopped, in addition to the numerous iterations required by Monte-Carlo based simulations. In order to deal

with this problem, SRIM introduces an approximation referred to as the Free Flight Path. It will adjust the distance between collisions depending on the energy, making it larger in the high energy range [10], [31]. This approximation will only evaluate the most significant collisions, consequently improving the efficiency of this program.

Regarding elastic collisions, the calculation of the stopping powers related to them is based on the Ziegler-Biersack-Littmark (ZBL) interatomic potential [10] and the scattering that they produce will be determined by the *Magic Formula*. On the other hand, electronic stopping powers are obtained by fitting and extrapolation of a large database of experimental results [32]. With respect to the treatment given to implantation-induced damage SRIM provides two different approaches, i.e. the full damage cascade calculation or the simplified Kinchin Pease model. The random numbers that characterize the consecutive collisions are independent to those determining the recoils of displaced particles [31]. Therefore, simulations carried out with different damage models will result in identical depth profiles. However, the modified Kinchin Pease model is limited to the calculation of the number of atomic displacements [32]. This approach reduces exponentially the computational cost of the simulations. Nevertheless, if detailed information of the damage profiles is needed, the full damage cascade model is recommended. With this approach, the trajectories of the recoiling particles are studied until their energy is lower than the threshold energy, below which they are considered to be stopped [31]. The energy transfer of the collisions, together with their position are recorded [32] and, later on, this information is displayed in various ways: 1-D and 3-D profiles, damage distribution in different planes and target materials, etc. Other functions offered by SRIM are the possibility of studying the sputtering of the substrate, running consecutive implantations and computing the final result, or adjusting manually some parameters like the displacement energy or the binding energies [31]. Moreover, the resulting depth profiles come together with the first order distribution moments that characterises them. This opens the possibility of using SRIM simulations as a source of data for potential implementation and improvement of statistical models, if the need of low execution times is essential.

Despite all these advantages, SRIM also presents some important limitations. The main constraints can be attributed to the lack of dose and temperature dependence effects on the resulting profiles. Since the targets are assumed to be amorphous, the final dopant concentrations are given normalised over dose, i.e. $(atoms/cm^3)/(atoms/cm^2)$ (see Fig. 3.6). In order to obtain the resulting impurity concentration, one will multiply by the desired implantation dose. Furthermore, simulations are carried out disregarding any effect of the temperatures under which the implantation takes place [31], which can lead to diffusion of impurities through the substrate.

All of the above, will introduce errors in the predictions given by SRIM. This two limitations are rather critical in the high energy range due to different reasons. On the one hand, in this energy range, damage build-up is usually higher, and the first implanted ions would have a greater impact on the following ones. Efforts towards

Fig. 3.6: Results given by a SRIM simulation of Al implantation into SiC at 380 keV. The four first distribution moments are also obtained in the simulation.

the avoidance of this aggravated lattice damage typically result in high temperature implantation, yet the effect of temperature will not be accounted for. Furthermore, assumes every target as amorphous, thus channeling effects present in crystalline SiC will be omitted, and ranges highly underestimated.

3.2.3 TCAD: Sentaurus

Technology Computer-Aided Design (TCAD) refers to the use of computers for the advanced simulation of semiconductor processes and devices, which improves the efficiency of their manufacturing. It offers detailed information on the results of processes, which go from the very first stages up to back-end steps. One of the simulators included in this category is Sentaurus, which in turn, incorporates several tools, among which, the following stand out: those that study the result of the main fabrication procedures, including *Sentaurus Process* and *Sentaurus Topography*, those that predict thermal, electrical and optical characteristics of the devices, e.g. *Sentaurus Device*, and an interface that enables the clear and interactive visualisation of the results, namely *Sentaurus Visual*. *Sentaurus Process* and *Sentaurus Visual* are the tools which lie within the scope of this thesis, since they are related to the simulation and representation of ion implantation depth profiles. With respect to ion implantation, *Sentaurus* offers a wide range of

possibilities to perform the simulations. Broadly, it relies upon two alternatives for these type of calculations: analytical and Monte-Carlo based simulations. As it occurred with the other simulators, the weight of computational costs against the accuracy of the results will determine which approach is best-suited in a particular scenario.

On the one hand, the analytical calculations (previously referred to as statistical), construct the depth profiles by interpolation of tabulated data. These tables give the distribution moments, which depend on the implanted species, dose, energy, rotation and tilt angles. The final profile can be fitted to different distributions: Gaussian, Pearson, dual Pearson, and even a Pearson with a linear exponential tail aiming to improve the description of the distribution tails. The data contained in these tables are obtained from different sources, including TRIM and *Sentaurus* calculations, literature and experimental results from SIMS measurements. This leads to a large and complete database that provides generally correct results. Of course, limitations discussed in Sec. 3.1, e.g. the dependency on implantation conditions and deviation of the predictions in the low concentration regions, cannot be fully avoided.

On the other hand, *Sentaurus* also allows the simulation of ion implantation based on Monte-Carlo models, with the so-called *Sentaurus MC*. Once again, these stem on the BCA and provide more accurate depth profiles, together with a detailed explanation of the physical phenomena that takes place during this process, e.g. stopping and damage effects. BCA enables to model the nuclear collisions and corresponding scattering by considering the interaction of the moving particle with only one atom per collision. The nuclear interaction between particles is modelled using the universal interatomic potential developed by Ziegler-Biersack-Littmark (ZBL), which takes the form [33], [34], (see Eqs. 2.4, 2.6):

$$V\left(r\right)=\frac{Z_1 Z_2 e^2}{r}[0.18175e^{-3.1998r/a_u}+0.50986e^{-0.94229r/a_u}+ \\ +0.28022e^{-0.4029r/a_u}+0.028171e^{-0.20162r/a_u}] \tag{3.12}$$

With the purpose of reducing the computational costs of determining the scattering of each collision, this simulator reduces the number of operations when evaluating the trajectory of the moving particle. This is accomplished by numerically solving the scattering integral over a wide range of values of the impact parameter p and the reduced energy ϵ. Then, these results are tabulated and come into use at each collision to determine the angle φ at which the atom recoils away and the energy loss (see Eq. 3.13) in a fast way.

$$T_n=\frac{4M_1M_2}{\left(M_1+M_2\right)^2}E_0\cos^2\varphi \tag{3.13}$$

For the electronic stopping, both non-local and local losses are considered. The former are calculated with the LSS formula and represent the energy losses caused by the

friction of the ions and therefore, depend on their velocity. On the other hand, local electronic losses, which represent the electrons transferred between the impinging ion and the atom, and therefore depend on the impact parameter, are calculated based on the Oen-Robinson model. Both parts will include correction factors set by default, but can also be adjusted manually [33], [34]. Induced damage can be represented both by the Kinchin Pease or full damage cascade models. Moreover, it can account for the diffusion of defects during implantation by the effects of dynamic annealing. Dechanneling caused by the damage accumulation in certain regions of the substrate is also taken into account.

Results provided by the implantation simulators in *Sentaurus Process* are outstanding in terms of accuracy (see Fig. 3.7) and computational costs with respect to others. Furthermore, it offers the possibility of automatically extracting the distribution moments of the profiles if these data cannot be found in *Sentaurus* tables. This approach would be an efficient way to build or improve data bases for statistical models previously addressed. Finding an algorithm that fits the resulting profiles to a statistical function with optimized distribution moments in the closest way possible is decisive. The Levenberg–Marquardt algorithm is the alternative used by *Sentaurus Process*.

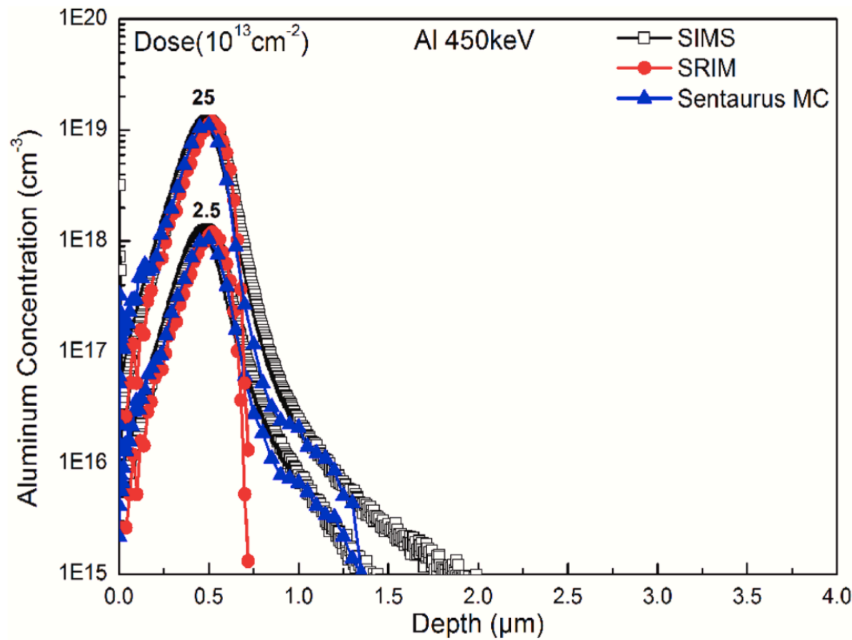

Fig. 3.7: Comparison of the depth profiles obtained from Al implantation into 4H-SiC at 450 keV and doses of 2.5 and 25 $\times 10^{13}$ cm^{-2} [35].

In an effort to further improve the computational costs, this tool also allows the

parallelization of simulations or part of them. This option is particularly useful when a large number of ions are to be implanted and consists on dividing the general process into individual parts with smaller doses. With parallelization, execution times can be considerably reduced and, although the profiles may not be identical than the non-parallelized process, results are equally good statistically [33].

Lastly, if something characterises this tool, is the freedom given to the user to adjust a vast majority of the parameters used in the models. Nevertheless, it provides the so-called Advanced Calibration, an option that contains preset models and parameters that are ideal for given conditions, e.g. ion implantation in 4H-SiC.

Chapter 4

Discussion of Results and Comparison between Simulators

In the previous chapter, different simulators for ion implantation were analysed, describing their characteristics, as well as some of their strengths and weaknesses. Now, the goodness of the results in each case will be evaluated from different perspectives, primarily accuracy, computational costs and flexibility. Moreover, they will be compared with each other in order to propose the best alternative to simulate ion implantation depth profiles. It should be pointed out that the main focus of this thesis is to evaluate the suitability of these algorithms for high energy ion implantation in 4H-SiC and, therefore, this chapter will lay a stronger emphasis on it.

4.1 Performance of *Implantor.m*

As it was explained in Subsec. 3.1.1, based on the fact that implantation profiles can be fitted to a Pearson IV distribution, a simulator was developed in Matlab by Y. Ju [1] at the Advanced Power Semiconductor Laboratory at ETH. It goes by the name *Implantor.m* (see Appendix A.1), and it extracts the corresponding distribution moments that describe the depth profile as a Pearson IV distribution. These moments are calculated from Eqs. 3.7 with the fitting parameters of Janson et al., shown in Table 3.1.

Only implanted species (Al or P), energy, dose and number of consecutive implantations can be selected, which will strictly limit the possibilities of *Implantor.m*. However, in the same way as other statistical approaches, the execution is instantaneous. The accuracy given by this model is evaluated by comparing its results with SIMS measurements [13].

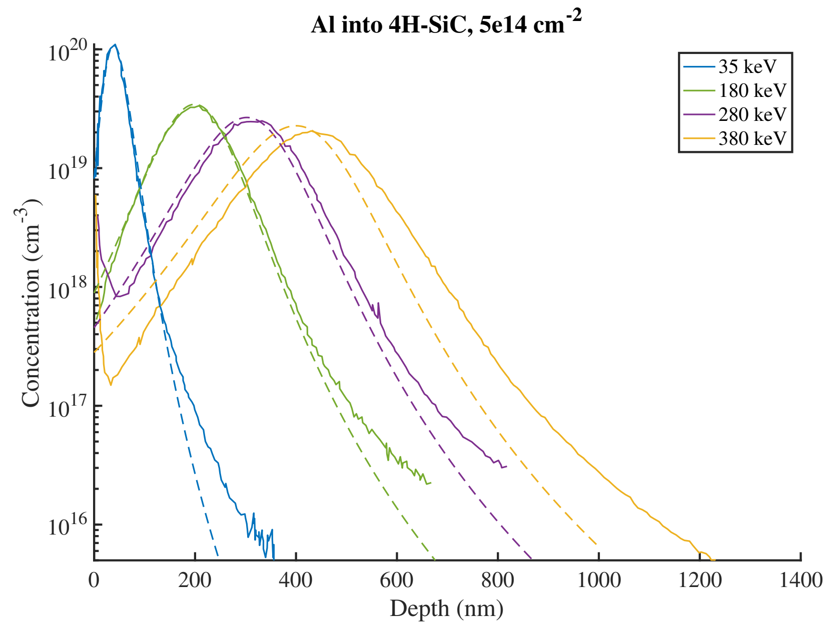

(a)

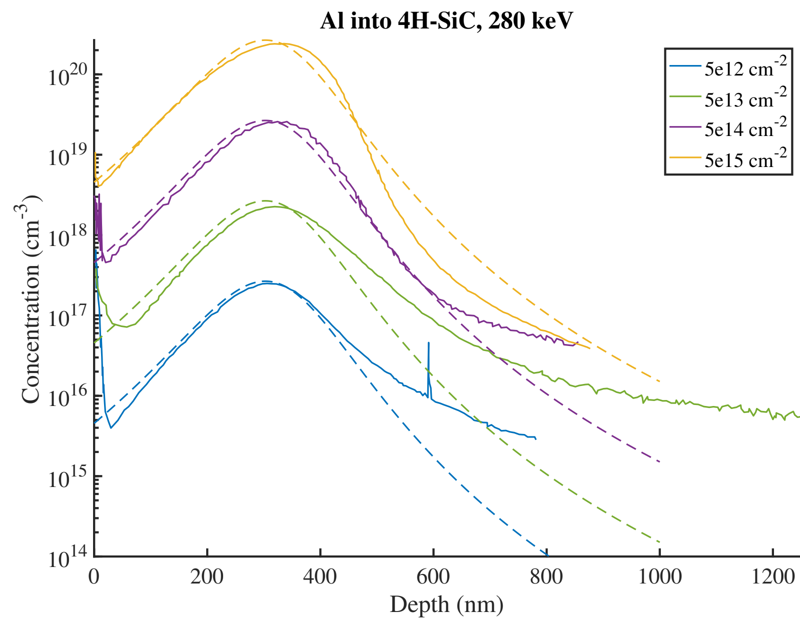

(b)

Fig. 4.1: Comparison of SIMS measurements (solid lines) [13] against *Implantor.m* simulations (broken lines). Figure (a) depicts the effect of energy in Al implantation into 4H-SiC and a dose $D = 5e14\ cm^{-2}$. Figure (b) shows the dose dependence of Al implantation into 4H-SiC at 280 keV.

Fig. 4.1a reveals that *Implantor.m* gives, overall, an acceptable approximation of the depth profiles. However, the tails of the distributions given by the simulator show significant deviations from the ones provided by SIMS. These parts of the profiles, where low dopant concentrations are located, represent the channeling and backscattering of the ions. They are strongly dependent on the direction in which the ions are implanted (and therefore on the tilt angle), energy, dose and temperature, among others (see Sec. 2.2). Since only an energy dependence was taken into account when extracting the fitting factors, other influences will be ignored. One that is particularly relevant is the dose effect, i.e. for higher doses, damage builds up and dechanneling is enhanced. In Fig. 4.1 the depth profiles obtained by SIMS show that the weight of the distribution tail decreases with dose (i.e. more pronounced negative slopes at the deep ranges), while *Implantor.m* does not change the shape of the profiles. An increase of the implanted dose will only change proportionally the concentration values, yet no further dose effects will be represented. This explains why when simulating high implanted doses (with respect to the one used to build the data bases that gave the fitting factors for this model, i.e. $\sim 1e14\ cm^{-2}$) *Implantor.m* gives higher concentrations than SIMS measurements in the deep range, by not considering the increase of dechanneling. Conversely, if lower

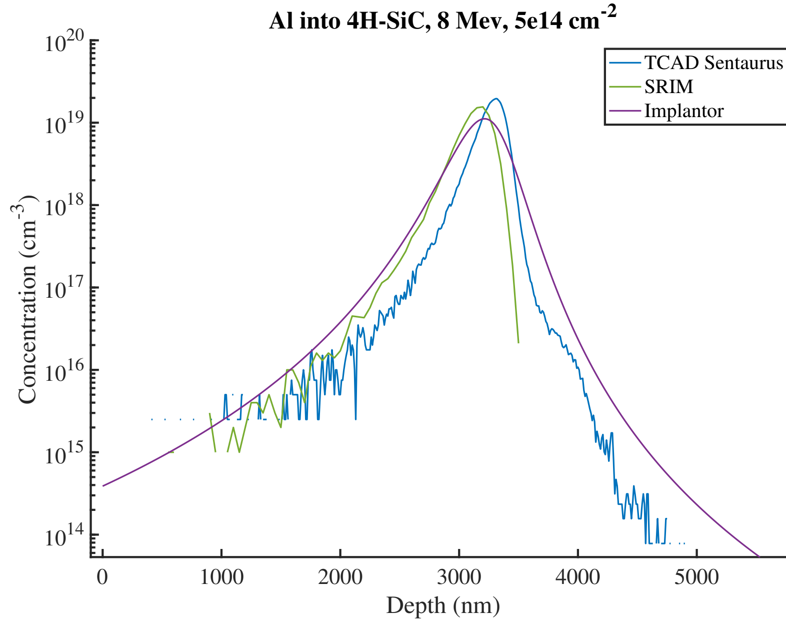

Fig. 4.2: Comparison of ion implantation depth profiles given by: *Sentaurus Process*, SRIM and *Implantor.m*. Simulation conditions were Al implantation into 4H-SiC, with energy $E = 8$ MeV and dose $D = 5e14\ cm^{-2}$.

doses are considered, this algorithm will estimate more damage than that produced by

a reduced dose and, therefore predicts lower concentrations for the tails of the profiles. However, at the high energy region, where implantation-induced damage plays an important role at high depths, the effects of channeling start fading. This explains why when simulating at the high energy range, *Implantor.m* gives surprisingly acceptable results (see Fig. 4.2). Additionally, it is important to note that Janson et al. parameters are calibrated for an energy range of 3.7 keV-3.2 MeV [8]. However, if the implantation conditions were changed, e.g simulating at higher temperatures or at different angles and doses, large deviations would be expected. This effect is represented in Fig. 4.3, where the predictions given by *Implantor.m* are compared to other sophisticated MC-BCA simulators. This figure reveals the incapability of the statistical approach to represent the effect of damage accumulation resulting from high implanted doses that lead to lattice disorder. The simulation is also unable to represent the consequences of high temperature implantation, which result in dopant diffusion and, depending on the dose and depth of study, can lead to lattice restoration or dechanneling enhancement [13].

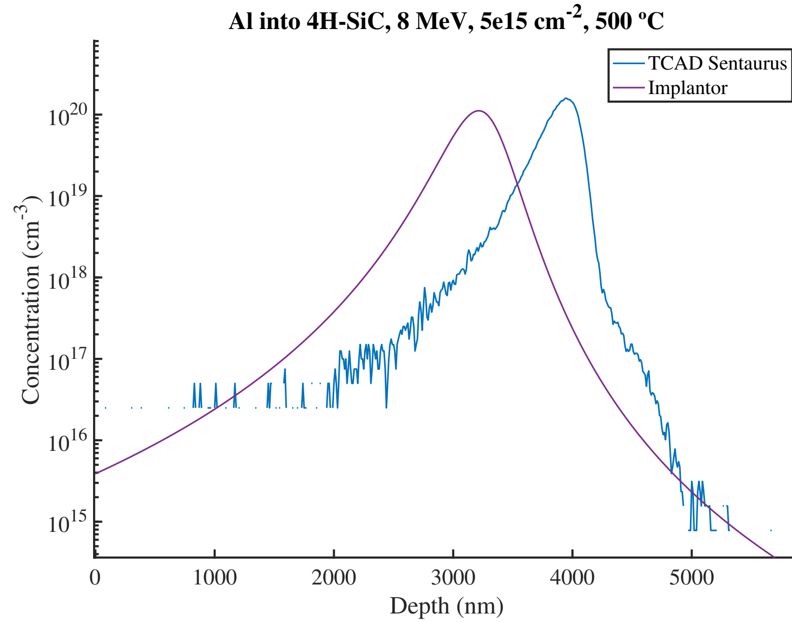

Fig. 4.3: Comparison of the predictions given by *Sentaurus Process* and *Implantor.m* in 4H-SiC for a high temperature Al implantation. Simulations were performed for $T = 500°C$, energy $E = 8$ MeV and dose $D = 5e15\ cm^{-2}$.

Moreover, results show that statistical models lack of sufficient robustness and are incapable of giving reliable predictions at even higher energies. The underestimation of the depths reached in the case of *Implantor.m* in Fig. 4.4 can be explained by the fact

that in this energy range, the ion can be seen as a bare nucleus moving through the target, with the interaction time being the limiting factor in the collisions. Therefore, the stopping power is reduced and the profiles shift to higher depths. This change in the principle of the interactions is deduced from Fig. 2.1. This drawback can be partly overcome by growing an extensive data set for high energies. Nevertheless, in these cases, profiles deviate significantly from the Gaussian distribution. The values for kurtosis and skewness are larger and the definition of the doping outlines based on the first four distribution moments becomes harder [36].

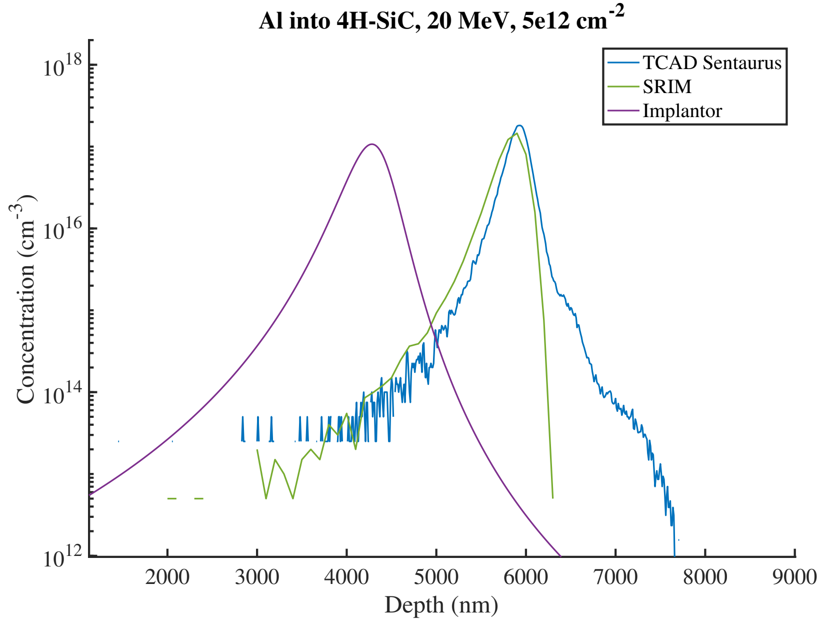

Fig. 4.4: Comparison of depth profiles predicted by *Sentaurus Process*, SRIM, and *Implantor.m* for a high energy Al implantation into 4H-SiC. The simulations were performed under an energy $E = 20$ MeV and dose $D = 5e12\ cm^{-2}$.

4.2 Performance of a dual Pearson based simulator

In an attempt to improve the accuracy of the profiles resulting from algorithms based on the Pearson IV distribution, the usage of the dual Pearson function is proposed. This approach has been proved to deal with channelling and asymmetries of the depth profiles more competently than the Pearson IV.

The dual Pearson consists of two weighted Pearson distributions that, summed up, give the final depth profile. One function accounts for the channeled and backscattered ions at the low concentration depths while the other represents the randomly scattered

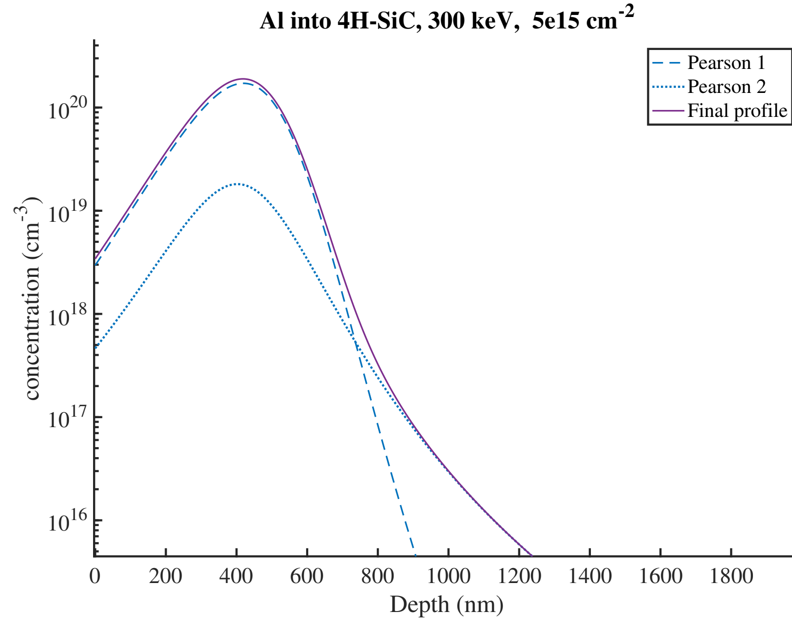

Fig. 4.5: Profile of Al implantation into 4H-SiC, with energy $E = 300$ keV and dose $D = 5e15\ cm^{-2}$, given by an algorithm based on the dual Pearson. Pearson 1 refers to the fraction of randomly moving ions and Pearson 2 refers to channeled and backscattered ions. Final profile is the sum of both distributions.

dopants that lie in the high concentration regions (see Fig. 4.5). Therefore, this distribution is described through nine statistical moments: R_{p1}, R_{p2}, ΔR_{p1}, ΔR_{p2}, γ_1, γ_2, β_1, β_2 and the dose ratio R. Due to the large number of parameters that need to be optimized, the fitting process becomes far more complex. Hence, in this work, the distribution moments were extracted from K. Mochizuki's graphs displayed in Fig. 4.6a [37]. From this graphs, the moments were fitted to a first or second degree polynomial dependent on the energy. The parameter R represents the weight of the non-channeled ions and it is tightly related to the dose range. For higher doses, due to the effects of damage accumulation, dechanneling is intensified. Therefore, the dose ratio corresponding to the non-channeled ions increases with dose. This relationship is exemplified in Fig. 4.6b. Although, ideally, one would obtain R as a function of both parameters, in the case of SiC (with no oxide mask), this parameter is only given as $R(E)$.

Following the same principles as *Implantor.m* an algorithm was developed in Matlab to simulate Al implantation depth profiles into 4H-SiC by means of the dual Pearson (see Appendix A.2). There is an obvious improvement in the representation of tails of the profiles, which come closer to those of SIMS. In other words, channeling effects are

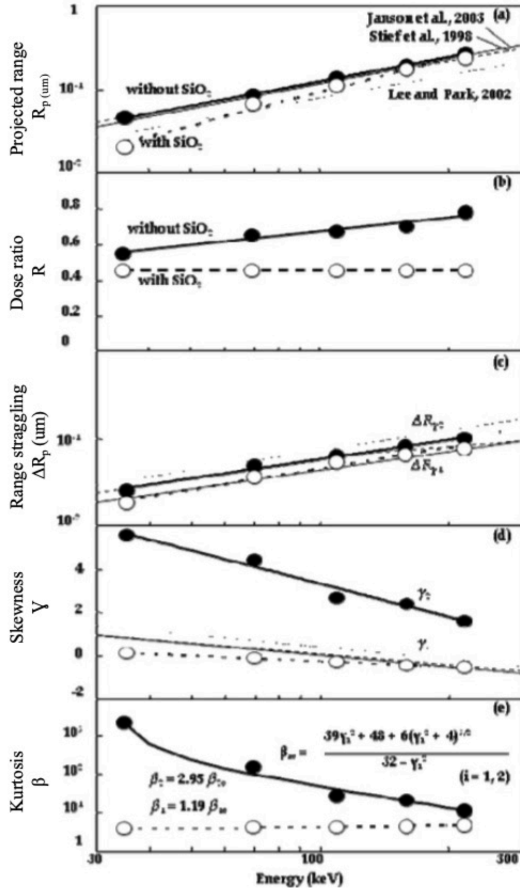

(a) Distribution moments of the dual Pearson for Al implantation into 4H-SiC given as a function of energy, by Janson et al. [8] and Stief et. al [7]. Graphs obtained from [37].

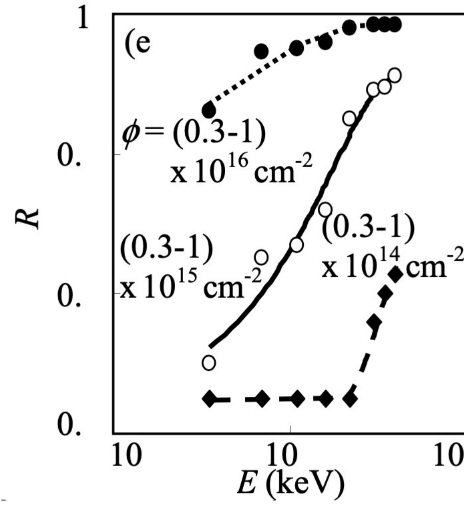

(b) Energy and dose dependence of the dose ratio R given by Mochizuki et al. [29] for Al implantation into 4H-SiC through a 35-nm $Si0_2$ film.

represented in a more accurate way, as it can be noticed in Fig. 4.7.

Despite this improvement, this algorithm fails to represent the characteristic dose effect, which determines the shape of the tails. This behaviour is a consequence of the fitting process that was followed, i.e. the distribution moments solely depend on the energy. The distribution moments used for this model are based on experiments with doping doses around $7e10^{13}$ cm^{-2}. As a consequence, when simulating at higher doses, the dual Pearson algorithm predicts more channeling than the SIMS profiles (see Fig. 4.8), since it does not take into account the damage build-up characteristic of this dose range. On the contrary, for lower doses, SIMS measurements will reflect that there is little damage on the lattice and significant tails arise. The simulation however is not

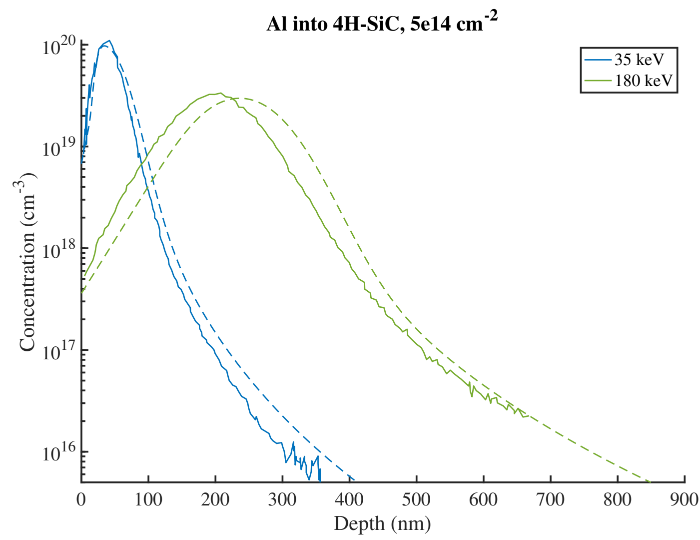

Fig. 4.7: Comparison between depth profiles of Al implantations into 4H-SiC given by a dual Pearson based simulator (broken lines) and SIMS (solid lines) [13]. Implantation was performed for different energies (35 kev, 180 keV) and a dose $D = 5e14\ cm^{-2}$.

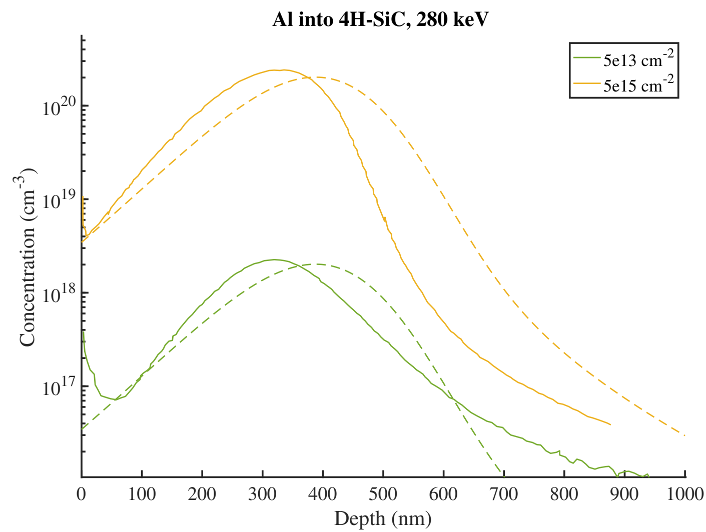

Fig. 4.8: Evaluation of the dose dependence in SIMS [13] (solid lines) and dual Pearson (broken lines) depth profiles of Al implantation into 4H-SiC, at 280 keV.

able to take this into account and underestimates the amount of channeling as shown in Fig. 4.8. Due to the fact that this algorithm takes a statistical approach, computation times are almost instantaneous. Nevertheless, different reasons denote that it is far from being the best approach to predict implantation depth profiles. Besides the limitations characteristic of statistical models, e.g. lack of flexibility with respect to implantation conditions, the methodology employed to obtain the distribution moments is rather imprecise. A more sophisticated fitting algorithm, able to withstand the complexity of optimizing all nine parameters, would be needed. Also, it would be necessary to make improvements regarding the treatment of the dose-dependence, at least with respect to the dose factor R, the critical point of the dual Pearson.

Hereunder, the results based on the Pearson IV and dual Pearson distribution will be compared to BCA simulations [37] in order to exemplify the main advantages and disadvantages between each other, some of which have already been introduced. The

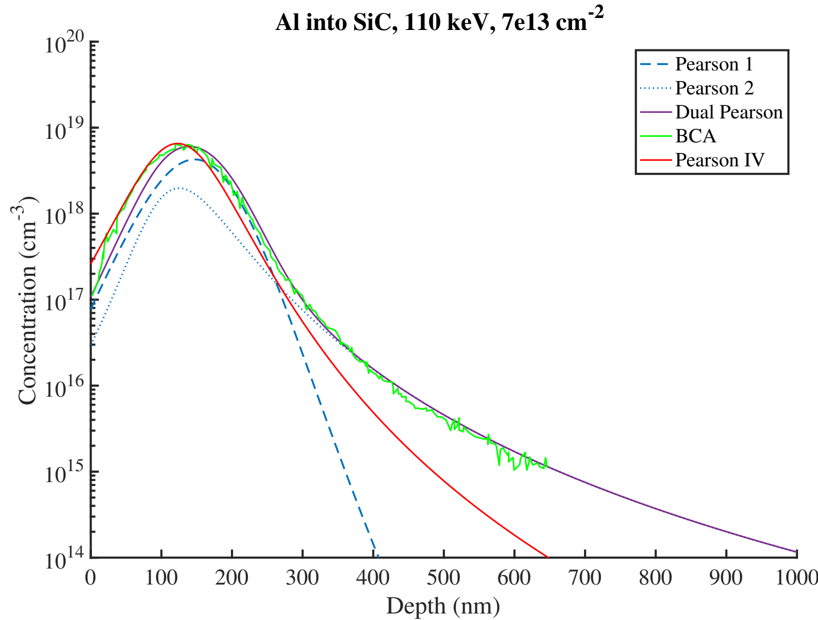

Fig. 4.9: Comparison of depth profiles resulting from Al implantation into 4H-SiC, at 110 keV and a dose $D = 7e13\ cm^{-2}$. BCA [37], Pearson IV [2] and dual Pearson simulations are represented.

first graph (see Fig. 4.9) also shows the weighted functions that compose the dual Pearson. It is noticeable how this approach depicts extraordinarily the tail of the profile while *Implantor.m* fails to do so. The latter uses solely a Pearson IV, thus no channeling effects are accounted for. Moreover, the flexibility of this distribution is limited and the asymmetries caused by backscattering and channeling effect are hard to represent.

Although implanting into symmetry directions (i.e. enhancing channeling) is being studied as an alternative to achieve deep implantation, usually tilt angles around 8°[8] are adopted in order to avoid this rather unpredictable phenomenon.

On the other hand, when changing the simulation conditions to slightly higher energies and doses, damage increases. Channeling effects become secondary and the differences between the tails given by the two approaches become less significant. At a certain point, usually when amorphization of the substrate is reached, the Pearson function that represents channeled ions will lose its meaning and the profile could be represented by a single Pearson. This can be deduced from Fig. 4.6b, where for high doses and energies, R saturates at its maximum value 1. Additionally, the fitting parameters used in *Implantor.m*, i.e. the single Pearson IV, were obtained with a much more advanced method than the approach used for the dual Pearson simulator. Therefore, excluding the deep ranges, *Implantor.m* will predict profiles that indeed adjust in a closer way to the reference distributions, in this case BCA simulations [37]. These are some of the reasons that question the superiority of the dual Pearson with respect to the Pearson IV function and can be observed in Fig. 4.10.

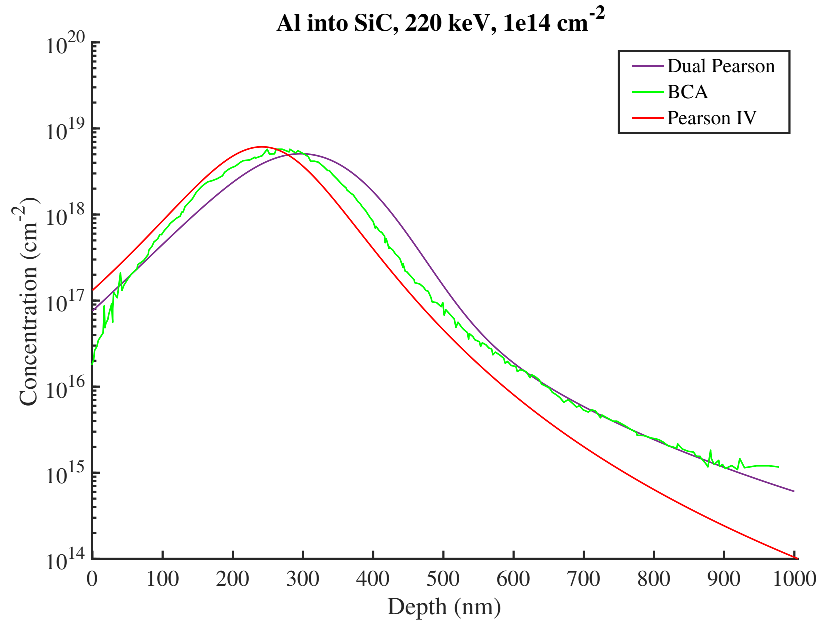

Fig. 4.10: Depth profiles resulting of Al implantation simulations into 4H-SiC, at 220 keV and a dose $D = 1e14\ cm^{-2}$. BCA [37], *Implantor.m* and dual Pearson simulations are represented.

These and other limitations stand out in the high energy range. Here, complex phenomena like the partial stripping of the ions or the increase of electronic and nuclear

stopping inflicted by implantation-induced damage lead to shallower profiles than those predicted by this dual Pearson based algorithm. Despite having extraordinary computational costs and being able to improve the representation of asymmetries, too large inaccuracies from the real profiles (see Fig. 4.11) rule out this model as an acceptable alternative for simulation of high energy ion implantation depth profiles. If computational costs were the limiting factor, the dual Pearson may still be the preferable option for the high energy range because of the explained arguments. If further improvements on the method for the extraction of the distribution moments are made, this function would be a promising alternative for representing depth profiles with large asymmetries. Of course, an extensive data base for the high energy range would be necessary to properly predict the final distributions.

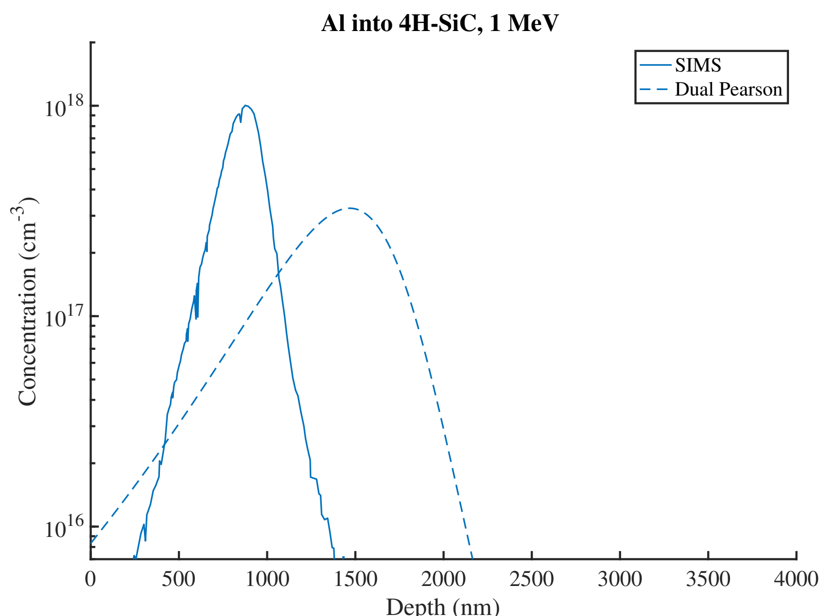

Fig. 4.11: Comparison of SIMS measurements [8] (solid line) and a dual Pearson based simulation (broken line) of Al implantation into 4H-SiC with energy $E = 1$ MeV and dose $D = 2.6e13\ cm^{-2}$.

4.3 Performance of SIIMPL

Simulation of Ion Implantation (SIIMPL), developed by M. Janson, is intended to simulate ion implantation related phenomena, e.g. dopant depth profiles, implantation-induced damage and Rutherford backscattering phenomena, among others. Initially, it was designed to study ion implantation in SiC, but an extended variety of amorphous

and crystalline targets was later included. This program follows the physical approach and is based on MC-BCA. Therefore, an improved prediction of the depth profiles is expected with respect to results seen in previous sections. On the other hand, execution times are considerably increased, thus this trade-off needs to be studied. In Fig. 4.12 SIMS [13] and SIIMPL profiles are compared. Throughout all the depth range, SIIMPL gives a close representation of the measurements. There is a clear improvement in the tail region compared to the Pearson IV approach. Although the dual Pearson made some progress regarding this matter, it deviated in other ranges of the profiles, due to the rough fitting and extrapolation of the distribution moments. SIIMPL gives proper predictions of the doping concentrations regardless of the depth region.

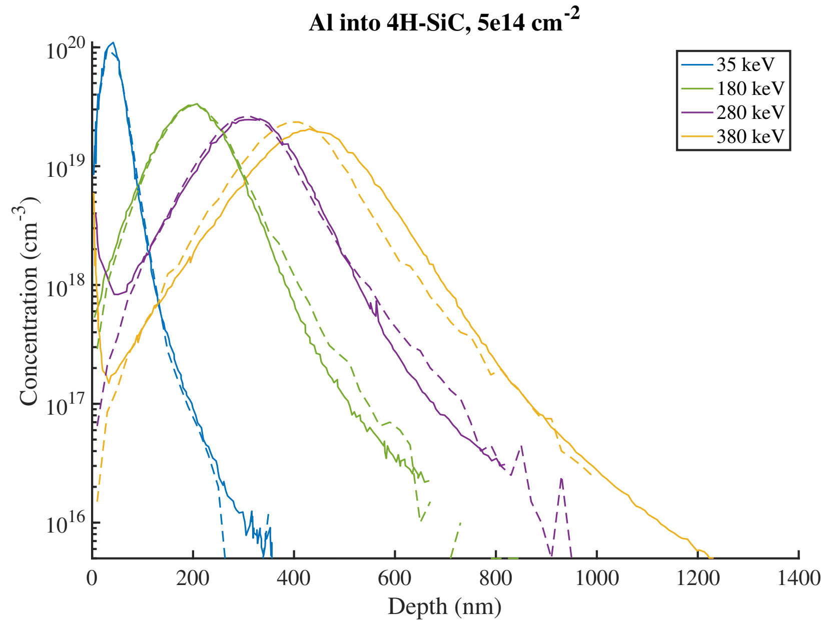

Fig. 4.12: Influence of energy in depth profiles of Al implantation into 4H-SiC with a dose $D = 5e14\ cm^{-2}$. SIIMPL simulations are represented by broken lines, while SIMS [13] measurements are represented by solid lines.

SIIMPL considers implantation-induced damage by calculating the probability of an ion colliding with an interstitial as:

$$P = c_a N_I / N, \tag{4.1}$$

where N is the atomic density of the target and N_I is the local density of interstitials calculated in the simulation. c_a is a semi-empirical parameter that is adjusted depending on the implantation direction and points out that damage may not be randomly

distributed through the sample, but rather affects each direction in a particular way. It represents effects like clustering and redistribution of point defects. However it is manually tuned through empirical evidence [2]. SIIMPL simulations have high computation times, hence the efficiency of this adjusting process is questionable. Fig. 4.13 shows ion implantations simulated with different doses and omitting this calibration step. This explains the deviations of the profiles, particularly at higher depths, where channeling takes place and the dose dependence plays an important role.

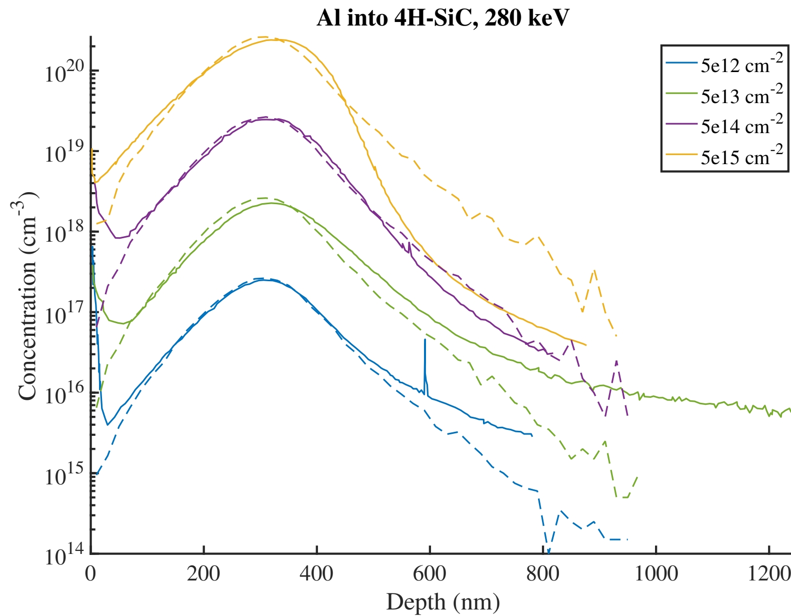

Fig. 4.13: Representation of Al implantation into 4H-SiC at 280 keV and different doses. Depth profiles were obtained by SIMS measurements [13] (solid lines) and SIIMPL simulations (broken lines).

In order to obtain precise results, the full damage cascade model is advantageous. Moreover, the number of Monte-Carlo iterations can be increased for more exact predictions. However, computational costs will worsen, and simulations in the range of 200-400 keV will take up to 4-5 hours. Execution time also increases with energy and for implantations of ~ 1 MeV, simulations of approximately 10 hours would take place. If these simulations are used in research fields, SIIMPL provides trustworthy predictions. However, if the goal is to improve the efficiency of the production process in an industrial scale, a faster simulator would be needed.

4.4 Performance of SRIM

This software developed by J. Ziegler aims to study the behaviour of ions when interacting with matter. It is particularly popular for ion implantation studies, for which the program TRIM is employed. It provides detailed information about the depth profiles of dopant species, their stopping powers and damage induced during the process. Its Monte-Carlo based simulations study the physical phenomena behind ion implantation, addressing the atomic interactions from the binary collision approximation perspective. Despite using physical models, SRIM is able to give precise predictions with reasonable execution times. From Fig. 4.14 one particular region stands out. While the lower and

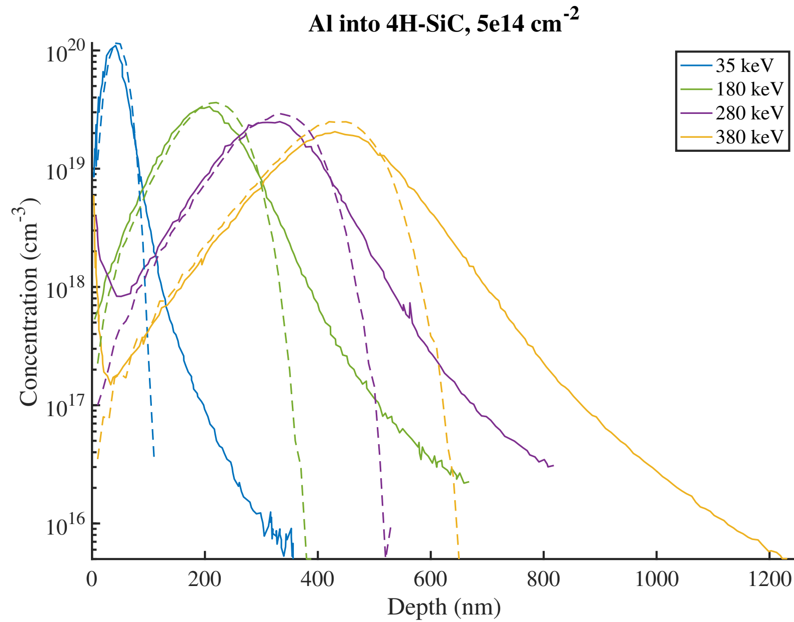

Fig. 4.14: Depth profiles of Al implantation into 4H-SiC given by SIMS [13] (solid lines) and TRIM simulations (broken lines). Implantation was performed at different energies and a dose $D = 5e14\ cm^{-2}$.

medium depths are predicted by TRIM with a high degree of accuracy, the tails of the distributions are far from being precise, since they give much lower concentrations than the ones obtained by SIMS measurements. These deviations can be attributed to the fact that TRIM considers every target as an amorphous substrate. Since amorphous targets do not have an ordered structure, they do not form well-defined channels into which the ions can be trapped and where the stopping is substantially lower. Consequently, dopants will be stopped considerably sooner, in contrast with the case of study, i.e. implantation into crystalline 4H-SiC. In this type of targets, as it was explained in Sec.

2.2, the incident ions can be channeled into symmetry directions, where they get 'stuck' between atom rows. Here, both nuclear and electronic stopping are minimized and, in consequence, channeled ions reach much higher depths. This is explains why in the simulations the tails of the profiles are completely neglected.

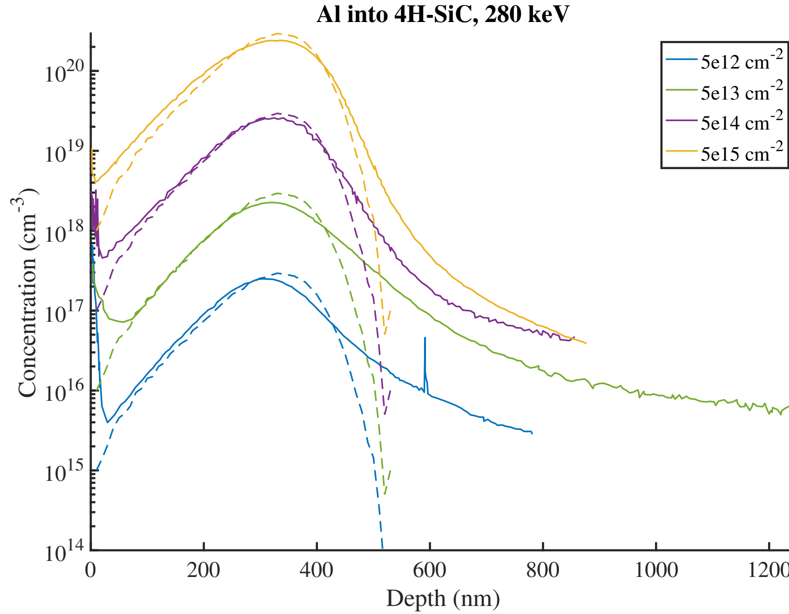

Fig. 4.15: Depth profiles given by Al implantation into 4H-SiC at 280 keV and different doses measured with SIMS [13] in solid lines. Broken lines represent the simulation by TRIM of implantation in the same conditions.

Moreover, the fact that all targets are considered as amorphous implies that no dose-effect will be taken into account. In an amorphous target, the atoms are not arranged in a particular order. Therefore, the displacements caused by previous ions will not have an effect on their trajectories. The dopants are assumed to move randomly through the sample, regardless of the implanted dose. For this reason, when several implantations are simulated maintaining constant the energy and varying the implanted dose, the profiles will be completely proportional (see Fig. 4.15). In fact, the units of concentration of the depth profiles given by TRIM are $(atoms/cm^3)/(atoms/cm^2)$ and the final doping concentration is obtained by multiplying by the corresponding dose (see Fig. 3.6). As it was explained in previous sections, for higher doses, implantation-induced damage builds up in the tails of the channels, leading to an increase of dechanneling rates. That is why SIMS measurements reveal less pronounced tails in the high depth region when dose increases, i.e. dechanneling enhancement. The inability to represent the dose-effect is another limitation that this simulator is restricted by.

Lastly, TRIM's performance is evaluated in the high energy range. With exception of the deeper region, this algorithm predicts implantation profiles with an acceptable degree of precision, as shown in Fig.4.16. Computational costs are also improved with respect to other physical approaches addressed so far. Simulations in the MeV range represented in Fig. 4.16 took around 1-2 hours, which is a reasonable time for simulators studying complex physical phenomena and a great improvement with respect to SIIMPL. In conclusion, SRIM provides good approximations of depth profiles with decent computational costs for low and medium depths. However, it presents a considerable drawback by assuming every target as amorphous. The tails of the distributions and the effect of implantation-induced damage will not be rightfully predicted. Considering that the goal in this particular case is to predict ion implantation depth profiles in crystalline 4H-SiC, this is a rather severe limitation. For this reason, SRIM is ruled out as a valid alternative for the simulation of ion implantation depth profiles in crystalline SiC.

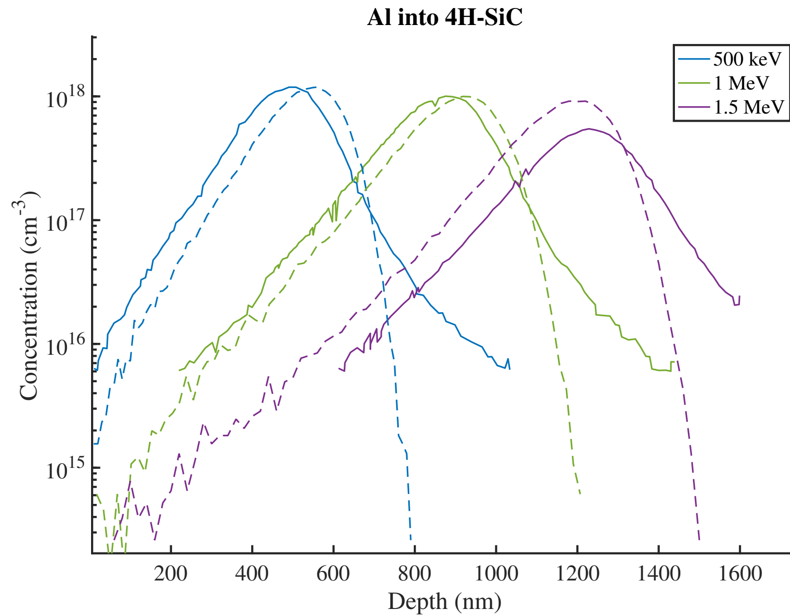

Fig. 4.16: Depth profiles of Al implantation into 4H-SiC at different energies and a dose $D = 2.6e13\ cm^{-2}$. SIMS measurements [8] are represented by solid lines and TRIM simulations by broken lines.

4.5 Performance of TCAD: *Sentaurus Process*

The use of computers for optimizing the design of semiconductor technology throughout the manufacturing process plays an important role in the industry. It allows to maximize the overall efficiency by simulating fabrication steps. Out of the many tools that this concept comprises, *Sentaurus Process* is the one that covers ion implantation simulation. *Sentaurus Process* generally follows the physical approach for simulations and it allows a thorough adjustment of the models and parameters used in them. This flexibility

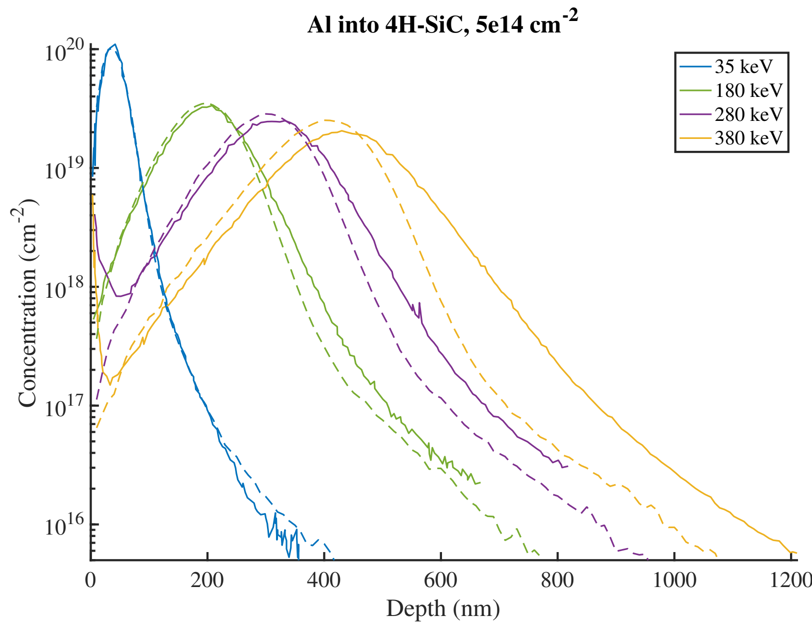

Fig. 4.17: Depth profiles of Al implantation into 4H-SiC by SIMS [13], represented by solid lines, and *Sentaurus Process* in broken lines. Implantation was performed for different energies and a dose of $D = 5e14\ cm^{-2}$.

results in rigorous predictions of the depth profiles, as shown in Fig. 4.17. Although deviations are still present in the high depth range, the shape of the simulations is accurate and shows an improvement with respect to other alternatives, e.g. SRIM.

This platform enables the customization of simulations, hence, depending on the criticality of the results, one could select the most suitable models. The flexibility of the simulations is remarkable and they will include the influence of complex phenomena, e.g. thermal vibrations. Accordingly, the dose effect is generally well represented by these simulations. In Fig. 4.18 it is observed how, when increasing the implanted dose, the negative slope of the profiles is intensified. In other words, higher doses result in accumulation of damage and enhancement of the dechanneling effect. This dose

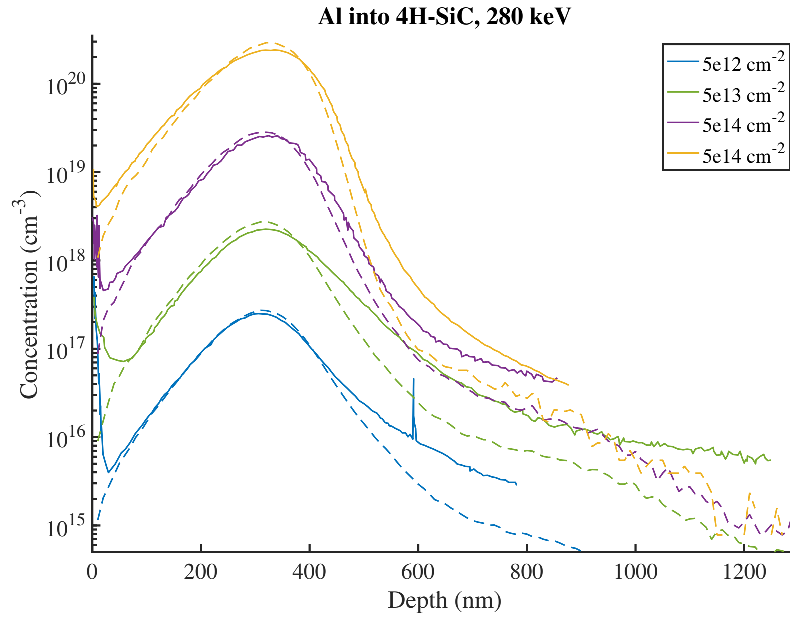

Fig. 4.18: Comparison of results given by *Sentaurus Process* (broken lines) and SIMS measurements [13] (solid lines) for an Al implantations into 4H-SiC. The dose dependence is reflected by maintaining the energy constant at $E = 280$ keV and adjusting the implanted dose.

dependence is reflected in SIMS depth profiles, which will present accentuated tails at lower doses, where a large fraction of the doping dose is channeled and reaches deeper regions. Although *Sentaurus Process* seems to underrate dopant concentrations at the high depth range, this dose dependence is visible and the precision at low and medium depths is outstanding. For implantations in the MeV range, this behaviour still stands. The depths and concentrations represented in Figs. 4.19 were calculated by *Sentaurus Process* in execution times below 1 hour. In terms of computational costs, this tool is highly superior than other physical simulators for 4H-SiC, e.g. SIIMPL.

Ultimately, *Sentaurus* gives remarkable predictions of ion implantation depth profiles and establishes a good compromise between precision and computational costs. Further advantages of this tool include the flexibility for thoroughly tailoring the simulations, thus leading to precise results. Moreover, *Sentaurus* includes simulations regarding other fabrication processes besides ion implantation. In this way, semiconductor manufacturing steps are unified over one platform, which, besides providing advanced and high-precision simulations, includes visualisation tools that represent the results of the processing and properties of such devices.

In Fig. 4.20 simulation alternatives based on the study of physical phenomena are

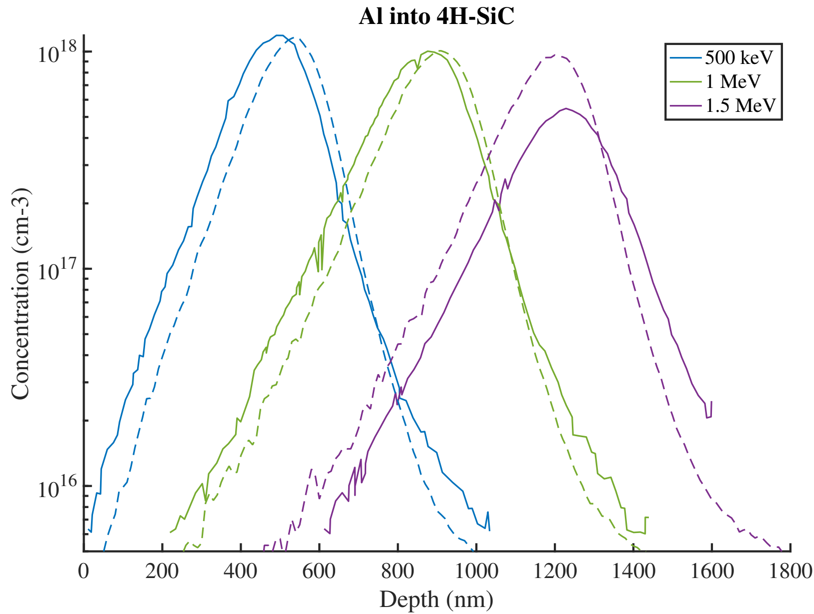

Fig. 4.19: Comparison of depth profiles given by *Sentaurus Process* simulations (broken lines) and SIMS measurements [8] (solid lines) for Al implantation into 4H-SiC in the high energy range. Implantation was performed for different energies and a dose $D = 2.6e13\ cm^{-2}$.

compared to SIMS measurements [13]. Here it is evident that SRIM presents the largest deviations with respect to SIMS measurements, since it only handles amorphous targets. On the other hand, it is interesting to point out that SIIMPL can give closer predictions to those of *Sentaurus* in particular cases. However, the deviations may stem from the fact that an 8° tilt was assumed in order to partly avoid channeling effects, however this might not be the actual direction used in the implantations measured with SIMS. Even so, computational costs of *Sentaurus Process* are only a 10% of those of SIIMPL. For the above-mentioned reasons, *Sentaurus Process* is proposed as the optimum alternative for the simulation of ion implantation depth profiles, including the high energy range.

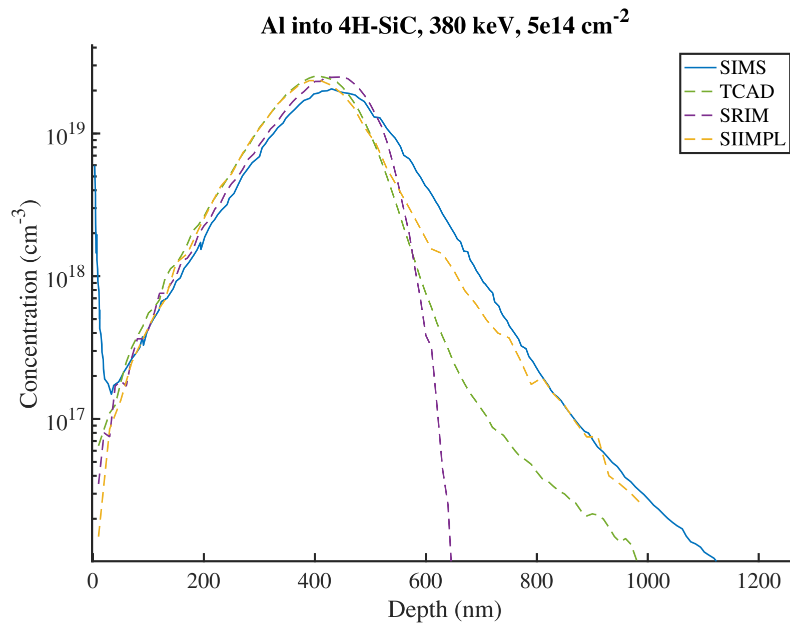

Fig. 4.20: Comparison of ion implantation depth profiles for an Al implantation into 4H-SiC given by TCAD (*Sentaurus Process*), SRIM and SIIMPL simulations (broken lines). SIMS measurement [13] of the corresponding implantation is also represented in the graph with a solid line. Implantation conditions were: energy $E = 380$ keV and dose $D = 5e14\ cm^{-2}$.

Chapter 5

Conclusion and Outlook

This thesis analysed different alternatives for the simulation of ion implantation depth profiles in 4H-SiC, aiming to find the best suitable option for the high energy range. The available programs were classified in two primary groups, i.e. statistical and physical models. Among these categories, some representative algorithms were tested and evaluated. In order to determine their goodness three main issues were addressed. Those are: (1) flexibility, (2) accuracy and (3) computational costs.

On the one hand, statistical models present instant execution times, yet their flexibility and accuracy are severely compromised. Among them, an algorithm based on the Pearson IV function showed faithful results at low depths. However, large deviations appeared in the tail of the distributions, due to the inability of this model to represent the asymmetries resulting of the channeling effect. As a solution to this problem, the dual Pearson distribution was proposed. It improves the precision of the predicted concentrations at higher depths. Despite this progress, and due to the fact that the method followed to extract the distribution moments was not quite rigorous and exhaustive, the accuracy of this new approach was, indeed, worse than the initial model based on a single Pearson. This suggests that, if no improvements are made in the fitting process, the dual Pearson has little advantages with respect to the single function. Moreover, although significant asymmetries are present in the high energy range, channelling effects are reduced. Both approaches, due to their statistical nature, are strictly constrained by implantation conditions and lack of an acceptable degree of generalization. This makes them uncompetitive for the current needs in this field.

On the other hand, physical models make outstanding progress regarding flexibility of the simulations, i.e. a large variety of implantation conditions can be simulated with reasonable precision. However, computational costs will considerably increase. Within this group, SIIMPL, SRIM and *Sentaurus Process* were tested and examined. The first one gave remarkably accurate predictions over the whole profile, yet it is severely limited by execution times, especially in the MeV range. On the contrary, SRIM improved computational costs, nonetheless it only supports amorphous targets. Lastly, *Sentaurus Process* presents an exceptional flexibility. Nearly every parameter can be adjusted to meticulously match the needs of every simulation. Moreover, it includes other tools that facilitate the unification of manufacturing simulation. It provides accurate predictions in

greatly reduced execution times. For all the reasons stated above, *Sentaurus Process* is here recognised as the optimal method for simulation of ion implantation depth profiles in the high energy range.

If computational costs were the limiting factor, efforts should focus on the improvement of the the dual Pearson approach. This could be accomplished by finding a sophisticated algorithm able to withstand the complexity of optimizing nine parameters, and by improving the experimental data base for the high energy range. However, the need of very precise control over the doping profiles of sophisticated structures in need of high energy ion implantation, such as the superjunction MOSFET, suggest that the accuracy of the simulations is the main concern. Consequently, a rising trend towards improving the advanced calibration proposed by *Sentaurus Process* for high energy ion implantation in 4H-SiC would be meaningful to finally achieve high precision predictions in this energy range. In fact, new releases of this tools already include this option and result in improvements in the precision of the results in this yet-to-be-mastered energy range.

Bibliography

[1] Y. Ju, “Fabrication and modeling of 4h-sic power mosfets,” Doctoral thesis, ETH Zurich, 2019.

[2] M. Janson, “Hydrogen diffusion and ion implantation in silicon carbide,” Doctoral thesis, KTH, Royal Institute of Technology, Department of Microelectronics, Information Technology, Materials, and Semiconductor Physics Laboratory, 2003.

[3] J. A. C. Tsunenobu Kimoto, “Device processing of silicon carbide,” in *Fundamentals of Silicon Carbide Technology*. John Wiley Sons, Ltd, 2014, ch. 6, pp. 189–276, ISBN: 9781118313534. DOI: `https://doi.org/10.1002/9781118313534.ch6`.

[4] F. Udrea, G. Deboy, and T. Fujihira, “Superjunction power devices, history, development, and future prospects,” *IEEE Transactions on Electron Devices*, vol. 64, no. 3, pp. 713–727, 2017. DOI: `10.1109/TED.2017.2658344`.

[5] P. Shenoy, A. Bhalla, and G. Dolny, “Analysis of the effect of charge imbalance on the static and dynamic characteristics of the super junction mosfet,” in *11th International Symposium on Power Semiconductor Devices and ICs. ISPSD'99 Proceedings (Cat. No.99CH36312)*, 1999, pp. 99–102. DOI: `10.1109/ISPSD.1999.764069`.

[6] W. Schustereder, D. Fuchs, O. Humbel, B. Brunner, and M. Pölzl, “Ion implantation challenges for power devices,” *AIP Conference Proceedings*, vol. 1496, pp. 16–21, Nov. 2012. DOI: `10.1063/1.4766479`.

[7] R. Stief, M. Lucassen, R. Schork, *et al.*, “Range studies of aluminum, boron, and nitrogen implants in 4h-sic,” in *1998 International Conference on Ion Implantation Technology. Proceedings (Cat. No.98EX144)*, vol. 2, 1998, 760–763 vol.2. DOI: `10.1109/IIT.1998.813778`.

[8] M. S. Janson, M. K. Linnarsson, A. Hallén, and B. G. Svensson, “Ion implantation range distributions in silicon carbide,” *Journal of Applied Physics*, vol. 93, no. 11, pp. 8903–8909, 2003. DOI: `10.1063/1.1569666`.

[9] J. F. Ziegler, *Srim.exe*, version 2013, 2013. [Online]. Available: `http://www.srim.org/SRIM/SRIMLEGL.htm`.

[10] J. Ziegler, “The stopping and range of ions in solids,” in *Ion Implantation Science and Technology (Second Edition)*, J. Ziegler, Ed., Second Edition, Academic Press, 1988, pp. 3–61, ISBN: 978-0-12-780621-1. DOI: `https://doi.org/10.1016/B978-0-12-780621-1.50005-8`.

[11] M. Nastasi and J. Mayer, *Ion Implantation and Synthesis of Materials.* Jan. 2006, ISBN: 978-3-540-23674-0. DOI: 10.1007/978-3-540-45298-0.

[12] E. Rimini, *Ion implantation : basics to device fabrication*, eng, 1st ed. 1995., ser. The Springer International Series in Engineering and Computer Science, 293. Boston, Massachusetts: Kluwer Academic Publishers, 1995, ISBN: 1-4615-2259-5.

[13] J. Müting, "Impact of dopant distribution on sic power mosfets," en, Ph.D. dissertation, ETH Zurich, Zurich, 2019. DOI: 10.3929/ethz-b-000388450.

[14] J. Lindhard, M. Scharff, and H. E. Schioett, "Range concepts and heavy ion ranges (notes on atomic collisions, ii)," 1963.

[15] T. T. Hlatshwayo, "Diffusion of silver in 6H-SiC," Doctoral thesis, University of Pretoria, 2010.

[16] P. Sigmund, "Low-velocity electronic stopping," Jun. 2004. DOI: 10.1007/978-3-540-44471-8_8.

[17] I. A. Akhiezer and L. N. Davydov, "Theory of electronic stopping of heavy ions in metals," *Soviet Physics Uspekhi*, vol. 22, no. 10, pp. 804–812, Oct. 1979. DOI: 10.1070/pu1979v022n10abeh005615.

[18] P. Sigmund and A. Schinner, "The bloch correction, key to heavy-ion stopping," *Journal of Applied Physics*, vol. 128, no. 10, p. 100 903, 2020. DOI: 10.1063/5.0015478.

[19] C. Park, K. Klein, A. Tasch, and J. ziegler, "Critical angles for channeling of boron ions implanted into single-crystal silicon," *Journal of the Electrochemical Society*, vol. 138, no. 7, pp. 2107–2115, 1991, ISSN: 0013-4651.

[20] A. Hössinger, "Simulation of ion implantation for ULSI technology," Doctoral thesis, Diss. Techn. Univ. Wien, 2000.

[21] K. Nordlund, S. J. Zinkle, A. E. Sand, *et al.*, "Improving atomic displacement and replacement calculations with physically realistic damage models," *Nature communications*, vol. 9, no. 1, pp. 1084–8, 2018, ISSN: 2041-1723.

[22] D. G. Ashworth, R. Oven, and B. Mundin, "Representation of ion implantation profiles by pearson frequency distribution curves," *Journal of Physics D: Applied Physics*, vol. 23, no. 7, pp. 870–876, Jul. 1990. DOI: 10.1088/0022-3727/23/7/018.

[23] H. Ryssel, G. Prinke, K. Haberger, K. Hoffmann, K. Müller, and R. Henkelmann, "Range parameters of boron implanted into silicon," *Applied physics*, vol. 24, pp. 39–43, 1981.

[24] K. Suzuki, "Analysis of ion implantation profiles for accurate process/device simulation: Ion implantation profile database based on tail function," *Fujitsu Scientific and Technical Journal*, vol. 46, pp. 307–317, Jul. 2010.

[25] L. Gong, S. Bogen, L. Frey, W. Jung, and H. Ryssel, "Analytical description of high energy implantation profiles of boron and phosphorus into crystalline silicon," *Radiation Effects and Defects in Solids*, vol. 127, no. 3-4, pp. 385–395, 1994. DOI: 10.1080/10420159408221046.

[26] Bratchenko, Dyuldya, and A. S. Bakai, "Enhanced phenomenological models of ion channeling contribution to doping profiles in crystals," *Condensed Matter Physics*, vol. 12, pp. 35–49, 2009.

[27] A. F. Tasch, H. Shin, C. Park, J. Alvis, and S. Novak, "An improved approach to accurately model shallow b and BF 2 implants in silicon," *Journal of The Electrochemical Society*, vol. 136, no. 3, pp. 810–814, Mar. 1989. DOI: 10.1149/1.2096748.

[28] K. Suzuki, "Analysis of ion implantation profiles for accurate process/device simulation: Analysis based on quasi-crystal extended lss theor," eng, *Fujitsu scientific & technical journal*, vol. 46, no. 3, pp. 318–326, 2010, ISSN: 0016-2523.

[29] K. Mochizuki and H. Onose, "Dual-pearson approach to model ion-implanted al concentration profiles for high-precision design of high-voltage 4h-sic power devices," in *Silicon Carbide and Related Materials 2007*, ser. Materials Science Forum, vol. 600, Trans Tech Publications Ltd, Feb. 2009, pp. 607–610. DOI: 10.4028/www.scientific.net/MSF.600-603.607.

[30] M. Janson, *SIIMPL: Simulation of ion implantation, users manual*, 2003.

[31] J. Ziegler, J. Biersack, and M. Ziegler, *SRIM, the Stopping and Range of Ions in Matter*. SRIM Company, 2008, ISBN: 9780965420716.

[32] W. J. Weber and Y. Zhang, "Predicting damage production in monoatomic and multi-elemental targets using stopping and range of ions in matter code: Challenges and recommendations," *Current Opinion in Solid State and Materials Science*, vol. 23, no. 4, p. 100 757, 2019, ISSN: 1359-0286. DOI: https://doi.org/10.1016/j.cossms.2019.06.001.

[33] *Sentaurus Process User Guide*, version R-2020.09, Sep. 2020.

[34] S. Tian, "Predictive monte carlo ion implantation simulator from sub-kev to above 10 mev," *Journal of Applied Physics*, vol. 93, no. 10, pp. 5893–5904, 2003. DOI: 10.1063/1.1565690.

[35] L. Sang, J. Xia, R. Jin, *et al.*, "Ion implantation of aluminum in 4h-sic epilayers from 90 kev to above 1 mev," *Solid-State Electronics*, vol. 172, p. 107 899, 2020, ISSN: 0038-1101. DOI: https://doi.org/10.1016/j.sse.2020.107899.

[36] J. Biersack, "Basic physical aspects of high energy implantation," *Nuclear Instruments and Methods in Physics Research Section B: Beam Interactions with Materials and Atoms*, vol. 35, no. 3, pp. 205–214, 1988, ISSN: 0168-583X. DOI: https://doi.org/10.1016/0168-583X(88)90272-8.

[37] K. Mochizuki, "One-dimensional models for diffusion and segregation of boron and ion implantation of aluminum in 4h-silicon carbide," in *Properties and Applications of Silicon Carbide*, R. Gerhardt, Ed., Rijeka: IntechOpen, 2011, ch. 2. DOI: 10.5772/14553.

Appendix A

A.1 Implantor.m

Algorithm developed by Y. Ju [1] at APS for the simulation of ion implantation depth profiles in SiC based on the Pearson IV approach.

```
1  clf
2  while true
3  try
4  s = input('please input a number, Al = 1, P = 2: ');
5  if s ~= 1 && s~=2
6  excep = MException('Pearson4:invalidInputs','invalid inputs
       ',s);
7  throw(excep)
8  end
9  break
10 catch ME
11 disp('invalid inputs');
12 end
13 rethrow(ME)
14 end
15 while true
16 try
17 y = input('please input the implant times: ');
18 break
19 catch ME
20 disp('invalid inputs');
21 end
22 rethrow(ME)
23 end
24 E = zeros(1:y);
25 Q = zeros(1:y);
26 Er = zeros(1:y); %keV
```

```
27 Rp = zeros(1:y);
28 del_Rp = zeros(1:y);
29 gamma = zeros(1:y);
30 beta_1 = zeros(1:y);
31 beta_0 = zeros(1:y);
32 p = 0;
33 if s == 1
34 a1 = 3.34; %nm
35 a2 = 0.42;
36 a3 = 113.6 .* 10^(-3);
37 a4 = 8.4 .* 10.^(-3);
38 b1 = 239; %nm
39 b2 = 484; %keV
40 b3 = 0.88;
41 c1 = 1.76;
42 c2 = 0.16; %keV^(-1/2)
43
44 c3 = 2.2;
45 c4 = 858; %keV
46 d1 = 1.5;
47 d2 = 126; %keV
48 Er = E; %keV
49 elseif s == 2
50 a1 = 1.43; %nm
51 a2 = 0.74;
52 a3 = 72.8 .* 10^(-3);
53 a4 = 6.8 .* 10.^(-3);
54 b1 = 188; %nm
55 b2 = 411; %keV
56 b3 = 0.97;
57 c1 = 0.86;
58 c2 = 0.02; %keV^(-1/2)
59 c3 = 1.4;
60 c4 = 476; %keV
61 d1 = 1.2;
62 d2 = inf; %keV
63 else
64 disp('this is an invalid input');
65 end
66 while true
67 try
```

```
68 E = input('please input energy matrix in keV: ');
69 break
70 catch ME
71 disp('invalid inputs');
72 end
73 rethrow(ME)
74 end
75 while true
76 try
77 Q = input('please input dose matrix in : ');
78 break
79 catch ME
80 disp('invalid inputs');
81 end
82 rethrow(ME)
83 end
84 range = [0 1000];
85 data_sets = cell(y,2);
86 for t = 1:1:y
87 Er(t) = E(t); %keV
88 Rp(t) = a1.*Er(t)^a2.*Er(t)^(a3.*log(Er(t))).*Er(t)^((-a4)
      .*(log(Er(t)))^2);
89 del_Rp(t) = b1./(1+(b2./E(t))^b3);
90 gamma(t) = (c1-c2.*sqrt(E(t))).*exp(-E(t)./c4)-c3.*exp(-c4
      ./E(t));
91 beta_0(t) = (48+39.*gamma(t)^2+6.*(gamma(t)^2+4)^1.5)./(32-
      gamma(t)^2);
92 beta_1(t) = beta_0(t).*(d1+2.5.*exp((-d2)./E(t)));
93
94 sub_Rp = Rp(t);
95 sub_del_Rp = del_Rp(t);
96 sub_gamma = gamma(t);
97 sub_beta = beta_1(t);
98 sub_Q = Q(t);
99 f = @(x) my_pear(x,sub_Rp,sub_del_Rp,sub_gamma,sub_beta,
      sub_Q);
100 if verLessThan('matlab', 'R2016a')
101 [x_abscissa, y_abscissa]=fplot(f, range, 10^3);
102 plot(x_abscissa, y_abscissa);
103 else
```

```
104 h=fplot(@(x) my_pear(x,sub_Rp,sub_del_Rp,sub_gamma,sub_beta
      ,sub_Q), range, 10^3);
105 set(gca, 'YScale', 'log')
106 ylim([1e15 1e20]);
107 x_abscissa=get(h,'XData').';
108 y_abscissa=get(h,'YData').';
109 end
110 data_sets{t,1} = x_abscissa;
111 data_sets{t,2} = y_abscissa;
112 hold on
113 end
114 for t= 1 : y-1
115 data_sets{t,2} = interp1(data_sets{t,1}, data_sets{t,2},
      data_sets{y,1},'spline');
116 data_sets{t,1} = data_sets{y,1};
117 end
118 added_data_y = sum([data_sets{:,2}],2);
119 plot(data_sets{1,1}, added_data_y);
120 xlabel('Depth (nm)'); % x
121 ylabel('concentration (cm-3)');
122 hold off
123 %depth = 0:5:data_sets{1,1};
124 cons = added_data_y;
125 fid = fopen('cons.txt','w');
126 fprintf(fid,'%6s %12s\r\n','depth','cons');
127 fprintf(fid,'%6.2f %.3e\r\n',[data_sets{1,1}.';cons.']);
128 fclose(fid);
129
130
131 function [p3] = my_pear(x,sub_Rp,sub_del_Rp,sub_gamma,
      sub_beta,Q)
132 C = 1/(2.*(5.*sub_beta-6.*(sub_gamma.^2)-9));
133 a = (-sub_del_Rp).*sub_gamma.*(sub_beta+3).*C;
134 B0 = (-(sub_del_Rp.^2)).*(4.*sub_beta-3.*(sub_gamma.^3)).*C
      ;
135 B2 = -(2.*sub_beta-3.*(sub_gamma.^2)-6).*C;
136 r = -(2+(1/B2));
137 n = (-r).*a.*(4.*B0.*B2-a.^2).^(-1/2);
138 m = (-1)/(2.*B2);
139 A = m.*r.*a./n;
```

```
140 %fun = @(x) exp((-n).*atan((x-sub_Rp)./A-n./r)).*(1+((x-
    sub_Rp)./A-n./r).^2).^(-m);
141 %p1 = integral(fun,-inf,+inf);
142 %p2 = (1./p1).*(exp((-n).*atan((x-sub_Rp)./A-n./r)).*(1+((x
    -sub_Rp)./A-n./r).^2).^(-m));
143 p1 = (abs(gammac(m+(n/2)*1i)/gammac(m)).^2)./(A.*beta(m
    -.5,.5*ones(size(m))));
144 p2 = Q.*(-p1).*(exp((-n).*atan((x-sub_Rp)./A-n./r)).*(1+((x
    -sub_Rp)./A-n./r).^2).^(-m));
145 p3 = p2.*10^7;
146 end
147
148
149
150
151
152
153 function [f] = gammac(z)
154 % Gammac by Pierce Brady
155 % Smart Systems Integration Group - SSIG
156 % Cork Institute of Technology, Ireland.
157 %
158 siz = size(z);
159 z=z(:);
160 zz=z;
161 f = 0.*z; % reserve space in advance
162 p=find(real(z)<0);
163 if ~isempty(p)
164 z(p)=-z(p);
165 end
166 g=607/128;
167 c = [ 0.99999999999999709182;
168 57.156235665862923517;
169 -59.597960355475491248;
170 14.136097974741747174;
171 -0.49191381609762019978;
172 .33994649984811888699e-4;
173 .46523628927048575665e-4;
174 -.98374475304879564677e-4;
175 .15808870322491248884e-3;
176 -.21026444172410488319e-3;
```

```
177 .21743961811521264320e-3;
178 -.16431810653676389022e-3;
179 .84418223983852743293e-4;
180 -.26190838401581408670e-4;
181 .36899182659531622704e-5];
182 z=z-1;
183 zh =z+0.5;
184 zgh=zh+g;
185 %trick for avoiding FP overflow above z=141
186 zp=zgh.^(zh*0.5);
187 ss=0.0;
188 for pp=size(c,1)-1:-1:1
189 ss=ss+c(pp+1)./(z+pp);
190 end
191 %sqrt(2Pi)
192 sq2pi= 2.5066282746310005024157652848110;
193 f=(sq2pi*(c(1)+ss)).*((zp.*exp(-zgh)).*zp);
194 f(z==0 | z==1) = 1.0;
195 %adjust for negative real parts
196 if ~isempty(p)
197 f(p)=-pi./(zz(p).*f(p).*sin(pi*zz(p)));
198 end
199 %adjust for negative poles
200 p=find(round(zz)==zz & imag(zz)==0 & real(zz)<=0);
201 if ~isempty(p)
202 f(p)=Inf;
203 end
204 f=reshape(f,siz);
205 end
```

A.2 Algorithm based on the dual Pearson

Modification of *Implantor.m* that uses the dual Pearson distribution for the representation of ion implantation depth profiles in SiC.

```
clf

while true
try
y = input('please input the implant times: ');
break
catch ME
disp('invalid inputs');
end
rethrow(ME)
end
E = zeros(1,y);
R = zeros (1,y);
Q = zeros(1,y);
Er = zeros(1,y); %keV
Rp = zeros(1,y);
del_Rp = zeros(2,y);
gamma = zeros(2,y);
beta_1 = zeros(2,y);
beta_0 = zeros(2,y);

p = 0;
mesh = 800;

while true
try
E = input('please input energy matrix in keV: ');
break
catch ME
disp('invalid inputs');
end
rethrow(ME)
end

```

```
35 while true
36 try
37 Q = input('please input dose matrix in : ');
38 break
39 catch ME
40 disp('invalid inputs');
41 end
42 rethrow(ME)
43 end
44
45
46 %coefs of the polynomials (of the stadistical moments)
      depending on the degree
47 %The order in the matrix is from higher order to lower
48 % for second degree coefsRp = [1.64599980275764e-07
      0.00125509468912408  0.00319839961443413 ];%
49 coefsRp = [0.00129717787914201,0.00122521911888428].*1000 ;
50 coefsR = [ 0.00111430077710390  0.562983594162327];
51
52 coefsDel_Rp1 = [0.000311373887905910
      0.0131607886413199].*1000;
53 coefsDel_Rp2 = [0.000407084728268032
      0.0161356621844527].*1000;
54
55 coefsGamma1 = [-0.00358285780542078 0.209727508175299];
56 coefsGamma2 = [-0.0214522936156417 5.89287264595618];
57
58
59 %Here beta(E) is not used. See analytical formula below
60 coefsBeta1 = [0.00340672955721532 3.95291049059344];
61 coefsBeta2 = [-8.90952496403542 1519.46824585287];
62
63
64 range = [0 2000];
65
66 data_sets = cell(y,2);
67 data_sets1 = cell(y,2);
68 data_sets2 = cell(y,2);
69
70
71 for t = 1:1:y
```

```
72
73 Er(t) = E(t); %keV
74
75 %second_degree = [E(t).^(2); E(t); 1 ];
76 first_degree = [E(t); 1 ];
77
78
79 % Rp1 = Rp2
80
81 R(t) = dot(first_degree,coefsR);
82 Rp(t) = dot(first_degree,coefsRp);
83
84 del_Rp(1,t) = dot(first_degree,coefsDel_Rp1);
85 del_Rp(2,t) = dot(first_degree,coefsDel_Rp2);
86
87 gamma(1,t) = dot(first_degree,coefsGamma1);
88 gamma(2,t) = dot(first_degree,coefsGamma2);
89 if gamma(2,t) >= 5.65
90     gamma(2,t) = 5.65;
91 end
92
93 beta_0(1,t) = (48+39.*gamma(1,t)^2+6.*(gamma(1,t)^2+4)^1.5)
      ./(32-gamma(1,t)^2);
94 beta_0(2,t) = (48+39.*gamma(2,t)^2+6.*(gamma(2,t)^2+4)^1.5)
      ./(32-gamma(2,t)^2);
95
96 beta_1(1,t) = 1.19.*beta_0(1,t);
97 beta_1(2,t) = 2.95.*beta_0(2,t);
98
99
100 if R(t) < 1
101     sub_R = R(t);
102 else
103     sub_R = 1;
104 end
105
106 sub_Rp = Rp(t);
107 sub_del_Rp1 = del_Rp(1,t);
108 sub_del_Rp2 = del_Rp(2,t);
109 sub_gamma1 = gamma(1,t);
110 sub_gamma2 = gamma(2,t);
```

```
111 sub_beta1 = beta_1(1,t);
112 sub_beta2 = beta_1(2,t);
113
114 sub_Q = Q(t);
115 %first pearson
116 p1 = @(x) dual_pear(x,sub_Rp,sub_del_Rp1,sub_gamma1,
       sub_beta1,sub_Q.*sub_R);
117
118 %second pearson
119 p2 = @(x) dual_pear(x,sub_Rp,sub_del_Rp2,sub_gamma2,
       sub_beta2,sub_Q.*(1-sub_R));
120
121
122 if verLessThan('matlab', 'R2016a')
123 [x_abscissa1, y_abscissa1]=fplot(p1, range, 10^3);
124 [x_abscissa2, y_abscissa2]=fplot(p2, range, 10^3);
125 plot(x_abscissa1, y_abscissa1);
126 hold on
127 plot(x_abscissa2, y_abscissa2);
128
129 else
130
131 h1 = fplot( p1, range, '--','MeshDensity', mesh);
132 set(gca, 'YScale', 'log')
133
134 ylim([1e15 1e20]);
135 x_abscissa1=get(h1,'XData').';
136 y_abscissa1=get(h1,'YData').';
137 hold on
138
139 if R(t) < 1
140 h2 = fplot(p2, range,':','MeshDensity',mesh );
141 x_abscissa2=get(h2,'XData').';
142 y_abscissa2=get(h2,'YData').';
143 h2.Color = h1.Color;
144 end
145 hold on
146 end
147
148 data_sets1{t,1} = x_abscissa1;
149 data_sets1{t,2} = y_abscissa1;
```

```
150
151 if R(t) < 1
152 data_sets2{t,1} = x_abscissa2;
153 data_sets2{t,2} = y_abscissa2;
154
155 %Obtain pearsons (1,2) at the same points
156 data_sets2{t,2} = interp1(data_sets2{t,1}, data_sets2{t,2},
        data_sets1{t,1},'spline');
157 else
158 data_sets2{t,2} = zeros(length(data_sets1{t,2}),1);
159 end
160 data_sets2{t,1} = data_sets1{t,1};
161
162 %Add both pearsons together
163 data_sets{t,2} = data_sets1{t,2} + data_sets2{t,2};
164 data_sets{t,1} = data_sets1{t,1};
165 plotF = plot(data_sets1{t,1}, data_sets{t,2});
166 plotF.Color = h1.Color;
167 hold on
168 end
169
170 for t= 1 : y-1
171 data_sets{t,2} = interp1(data_sets{t,1}, data_sets{t,2},
       data_sets{y,1},'spline');
172 data_sets{t,1} = data_sets{y,1};
173 end
174
175 added_data_y = sum([data_sets{:,2}],2);
176 plot(data_sets1{y,1}, added_data_y);
177 xlabel('Depth (nm)'); % x
178 ylabel('concentration (cm-3)');
179 hold off
180 %depth = 0:5:data_sets{1,1};
181 cons = added_data_y;
182 fid = fopen('cons.txt','w');
183 fprintf(fid,'%6s %12s\r\n','depth','cons');
184 fprintf(fid,'%6.2f %.3e\r\n',[data_sets1{y,1}.';cons.']);
185 fclose(fid);
186
187
```

```
188 function [p3] = dual_pear(x,sub_Rp,sub_del_Rp,sub_gamma,
       sub_beta,Q)
189 C = 1/(2.*(5.*sub_beta-6.*(sub_gamma.^2)-9));
190 a = (-sub_del_Rp).*sub_gamma.*(sub_beta+3).*C;
191 B0 = (-(sub_del_Rp.^2)).*(4.*sub_beta-3.*(sub_gamma.^3)).*C
       ;
192 B2 = -(2.*sub_beta-3.*(sub_gamma.^2)-6).*C;
193 r = -(2+(1/B2));
194 n = (-r).*a.*(4.*B0.*B2-a.^2).^(-1/2);
195 m = (-1)/(2.*B2);
196 A = m.*r.*a./n;
197 %fun = @(x) exp((-n).*atan((x-sub_Rp)./A-n./r)).*(1+((x-
       sub_Rp)./A-n./r).^2).^(-m);
198 %p1 = integral(fun,-inf,+inf);
199 %p2 = (1./p1).*(exp((-n).*atan((x-sub_Rp)./A-n./r)).*(1+((x
       -sub_Rp)./A-n./r).^2).^(-m));
200 p1 = (abs(gammac(m+(n/2)*1i)/gammac(m)).^2)./(A.*beta(m
       -.5,.5*ones(size(m))));
201 p2 = Q.*(-p1).*(exp((-n).*atan((x-sub_Rp)./A-n./r)).*(1+((x
       -sub_Rp)./A-n./r).^2).^(-m));
202 p3 = p2.*10^7;
203 end
204
205
206
207
208
209
210 function [f] = gammac(z)
211 % Gammac by Pierce Brady
212 % Smart Systems Integration Group - SSIG
213 % Cork Institute of Technology, Ireland.
214 %
215 siz = size(z);
216 z=z(:);
217 zz=z;
218 f = 0.*z; % reserve space in advance
219 p=find(real(z)<0);
220 if ~isempty(p)
221 z(p)=-z(p);
222 end
```

```
223 g=607/128;
224 c = [ 0.99999999999999709182;
225 57.156235665862923517;
226 -59.597960355475491248;
227 14.136097974741747174;
228 -0.49191381609762019978;
229 .33994649984811888699e-4;
230 .46523628927048575665e-4;
231 -.98374475304879564677e-4;
232 .15808870322491248884e-3;
233 -.21026444172410488319e-3;
234 .21743961811521264320e-3;
235 -.16431810653676389022e-3;
236 .84418223983852743293e-4;
237 -.26190838401581408670e-4;
238 .36899182659531622704e-5];
239 z=z-1;
240 zh =z+0.5;
241 zgh=zh+g;
242 %trick for avoiding FP overflow above z=141
243 zp=zgh.^(zh*0.5);
244 ss=0.0;
245 for pp=size(c,1)-1:-1:1
246 ss=ss+c(pp+1)./(z+pp);
247 end
248 %sqrt(2Pi)
249 sq2pi= 2.5066282746310005024157652848110;
250 f=(sq2pi*(c(1)+ss)).*((zp.*exp(-zgh)).*zp);
251 f(z==0 | z==1) = 1.0;
252 %adjust for negative real parts
253 if ~isempty(p)
254 f(p)=-pi./(zz(p).*f(p).*sin(pi*zz(p)));
255 end
256 %adjust for negative poles
257 p=find(round(zz)==zz & imag(zz)==0 & real(zz)<=0);
258 if ~isempty(p)
259 f(p)=Inf;
260 end
261 f=reshape(f,siz);
262 end
```

A.3 *Sentaurus Process*

Simulation of ion implantation depth profiles in 4H-SiC with *Sentaurus Process*.

```
Advanced Calibration 4H-SiC
# Initialize grid
#
line x loc = 0 tag = top spac= 0.01
line x loc= 2.0 tag = bottom spac= 0.01
#Asign structure (4H-SiC , default)
#
region SiliconCarbide xlo = top xhi= bottom
init miscut.tilt= 8 miscut.toward= {1 1 0}
#Simulate implantation
#
implant @species@ energy = @energy@ temperature = @temp@<C>\
dose = @dose@ tilt= 0
sentaurus.mc particles = 100000 info = 2
#Save
#
struct_tdr= SiC_Implant_tilt8_@species@_D@dose@_E@energy@_T@temp
```